「光・電子デバイス用ヘテロエピタキシャル GaN および GaAs の物性に関する研究」

Chapter 1

Introduction

In this dissertation, two heteroepitaxial systems consisting of, 1) GaN layer grown on sapphire substrate (GaN/sapphire) and 2) GaAs layer grown on Si substrate (GaAs/Si) are the target materials prepared for investigation.

1.1 Background

GaN/sapphire:

Maruska and Tietjen have first reported the growth of single crystalline GaN which has direct transition band structure with the bandgap energy of about 3.39 eV at room temperature on sapphire substrate by hydride vapor phase epitaxy (HVPE) in 1969 [1].

Since the first demonstration, group III nitride based wide-band-gap semiconductors of GaN, AlGaN and InGaN have been extensively studied due to the importance of the optical devices in the blue-to-ultraviolet (UV) regions, and the electronic devices for high power, high frequency, and high temperature applications.

In past several years, a number of notable progress have been reported in the fundamental growth techniques. A great advance in crystal growth was achieved by using a low-temperature buffer layer by metal organic chemical vapor deposition (MOCVD) [2]. The first p-type GaN was grown in 1989 by Amano and co-workers [3], by MOCVD using Mg as dopant. As-grown p-type GaN had a high resistivity but it is possible to achieve substantial p-type conductivity by a low energy electron beam irradiation (LEEBI) [3]. Nakamura and co-worker [4] successfully developed p-type conductivity by a thermal annealing which is suitable for a mass production rather than LEEBI method. The n-type conductivity was found to be controled by flowing SiH_4 during MOCVD growth in combination of a low-temperature buffer layer [5].

The blue and UV wavelengths are technologically important region for optical devices. At present, semiconductor optical devices in the wavelength ranges between infrared (IR) to green are operated by using As-based and P-based cosines semiconductor materials. For example, the wavelength of red range is realized by using AlGaAs-based and that of orange to yellow range is realized by using AlGaP-based material. If this range can be extended into the blue wavelength, three primary colors of the visible spectrum which may have a major impact on full-color imaging and graphics applications by only using compound semiconductors. Furthermore, GaN laser diodes (LDs) are favored for high density optical recording (compact discs: CDs, digital versatile discs: DVDs), photolithography.

Figure 1.1 shows the relationship between lattice constants and wavelengths corresponding to bandgap energy of major III–V compound semiconductors. The lattice constants of nitrides are calculated assuming that each crystal forms a cubic lattice: i.e. the lattice constants a_{cubic} is given by

$$a_{cubic} = \sqrt[3]{\sqrt{3} \times a_W^2 \times c_W}, \tag{1.1}$$

where a_W and c_W are the a- and c-axis lattice constants of wurtzite lattice structure, respectively. Among many III–V semiconductors, it is clear that group-III nitrides are located at different area in Fig. 1.1, that is, nitride-based semiconductors cover almost visible and UV regions and smaller lattice constants.

From the view point of material physical parameters, GaN is much different from more traditional semiconductors like Si or GaAs.

One of most interesting feature of GaN is that it is thought to have a hexagonal crystal since no other semiconductor laser diodes with wurtzite crystal have not been developed. Though the cubic crystal has been studied in recent years, it still does not have good quality compared to that of hexagonal crystal [6].

The large band gap (see Fig. 1.1) makes nitrides suitable for high power and high temperature applications [7, 8]. The magnitude of the critical field for breakdown voltage which is very important parameter for the design of bipolar and field-effect devices may be high and is preferred for high power devices. Furthermore GaN produces a negligible concentration of charge carriers at room temperature.

In comparison with conventional cubic phase of GaAs, GaN possesses larger effective masses in both electron and holes which affect transport properties. In case of laser diodes, the threshold current density of hexagonal GaN quantum-well (QW) laser diodes is intrinsically much higher than that of GaAs QW [9].

The large mismatch in the covalent radii of gallium (r_{Ga}=1.26 Å) and nitrogen (r_N=0.75 Å), and the electron negativity of gallium (1.13) and nitrogen (3.0) as shown in Table 1.3 play an important role in defect formation and impurities doping [10, 11]. Neugebauer and Van de Walle [10] investigated the consequences of this mismatch on defect formation energies for the example of the gallium antisite, where a particularly strong effect is observed. By replacing a nitrogen atom with a gallium atom the Ga–N bonds replaced by Ga–Ga bonds. If atomic relaxation is allowed, the four neighboring Ga atoms move outerward, reducing the strain in the Ga–Ga bond. This atomic relaxation accompanied by an energy gain of 4.2 eV which is about 3 times larger than typical relaxation energies for defects in GaAs [12] or ZnSe [13].

The large exciton binding energy (28 meV at room temperature) which is larger than k_BT at room temperature and effective electron mass may be expected important for manybody Coulomb interaction between the carriers [14, 15, 16]. The manybody Coulomb interaction will lead to the energy bandgap renormalization or narrowing [17]. This strong excitonic process have recently been reported to give rise to optical gain with excitation intensities up to 5 MW·cm^2 [18].

Nitrides have large elastic constants, which indicates the strong bond between the nitrogen and each column III atom. Thus the nitrides exhibit superior thermal and chemical stability and physical hardness. Moreover, nitrides devices are harmless, because nitrogen is in the principle constitute of the air.

Today, high luminous blue and green light emitting diodes (LEDs) fabricated based on group III nitrides (blue-LED and blue-green-LED) have become commercially available [19, 20, 21]. Looking at the historical development, the emergence of the GaN laser diodes have been quite unusual. Pulsed laser diodes with operating voltage of the order of 20 V were demonstrated in 1996, soon after this a life time of several 1000 h was obtained under continuous-wave (cw) operation in 1997. The market introduction of blue-violet GaN lasers has been predicted for the end of 1998 [22].

GaAs/Si:

Since the first report of successful heteroepitaxial growth of GaAs on Si substrate [23, 24] in 1984, the heteroepitaxial growth of III–V semiconductors on Si substrate has been continuously developed in the past decade. At the time of initial realization of cw operation of laser diodes the device life time was of the order of seconds and subsequenty was increased from minutes to several hundred hours in 1993. The improvement of the laser diodes was achieved through systematic research and development based on growth techniques and device structure. For example, the strained-layer superlattices (SLSs) [25], in-situ [26] or ex-situ [27] thermal annealing are effective to reduce the dislocations. The selective area growth was also useful for reducing the dislocation

density [28]. The post-growth patterning [29], the undercut GaAs/Si (UCGAS) proposed by Sakai *et al.* [30] are effective to reduce both the dislocation density and the residual thermal stress. However, up to now no convincing success of GaAs-based laser diodes on Si substrate has been reported since 1993. The amount of progress will depend on the effort with which the exist problems are tackled.

This structure GaAs/Si is very fashionable material for future opto electronic integrated circuits (OEICs) because of the possibility of combining the highly developed Si ultra large scale integrated circuits (ULSIs) and the GaAs-based LEDs or LDs. These devices, where Si ULSI cicuits are optically interconnected between them, realize the high speed data communications without delay becasue the optical data transfer is not affected by a electromagnetic interface. Moreover substantial benefits of GaAs/Si are its application to solar cells. The advantages of GaAs/Si tandem solar cell shows not only theoretical efficiency as high as 30 % but also low-cost, large-area, mechanical hardness substrate and high thermal conductivity. Soga *et al.* reported a conversion efficiency as high as 20.6 % with AlGaAs/Si tandem solar cell [31, 32].

Today, the application of GaAs/Si to majority carrier devices like high electron mobility transistors (HEMTs) [33, 34], metal semiconductor field effect transistors (MESFETs) [35, 36] have obtanied prominent success. The characteristics of GaAs devices on Si substrate are comparable to those on GaAs substrate and GaAs devices on Si substrate are sufficiently substitutable for those on GaAs substrate in the application to both ICs and discreate devices. This advancement is much indebeted that the majority carrier devices are not affected by the dislocations and the total epitaxial layer is relatively thin for these devices and cracks are not generated. It can be concluded that the minority carrier devices like LEDs or LDs are easily affected by dislocations in comparion with majority carrier devices.

GaN/sapphire and GaAs/Si heteroepitaxial techniques:

It seems that the main aim to develop the heteroepitaxial techniques in GaN/sapphire and GaAs/Si is little different. In case of GaAs/Si, the aim is set to the integration of the advantages of the individual materials (GaAs, Si), however, this is not the case in GaN/sapphire since the idea for integration does not mature in this material. However, there can be no doubt that rich opportunities for heteroepitaxial engineering exist.

Besides the main aim, one of the major difficulties to produce and control a high quality GaN layer or a GaAs layer is the lack of an ideal substrate material (lattice matched substrates). Therefore, the both GaN/sapphire and GaAs/Si heteroepitaxial material systems suffer from two major problems due to the difference in material parameters between the substrate (sapphire or Si) and the epitaxial layer (GaN or GaAs) as listed follows.

1) The generation of high density of dislocations due to the mismatch of lattice constants as shown in Fig. 1.1.

2) The large biaxial stress in epitaxial layer generated during cooling from the growth temperature due to the difference in the thermal expansion coefficients as shown in Table 1.1 (compressive stress: GaN/sapphire, tensile stress: GaAs/Si).

In general, GaN films are much poorer in quality than common GaAs or Si and thus very suprising large number of defects as $\sim 10^{10}$ cm^{-2}, which is two order magnitude larger than that of GaAs/Si as $10^6 - 10^8$ cm^{-2}, even in carefully prepared layers of GaN on sapphire. There is a big marked differences between GaN-based devices and GaAs-based devices especially lasers. Even this inferior situation in GaN, it is a miracle which has been posed many times how is it possible for GaN-based LEDs and lasers to operate for a long time. For GaAs LDs (not GaAs/Si), which has much higher crystal quality, the development took of the order of 10 years with numerous groups working on the problems. Contrary to GaN-based devices, over a decade have past since Deppe *et al.* [37] reported the first successful room-temperature cw operation from an AlGaAs/GaAs single quantum well (SQW) LD grown on Si substrate. However, the life time of devices are still around several 100 h which is one order magnitude smaller than that of GaN-based LDs although the several new approaches and efforts have been reported, e.g., use of

a strained layer supper lattice [38], in-situ and ex-situ thermal cycle annealing (TCA) [39] and combination of these techniques [40]. The reasons of these rapid degradation is the formation and propagation of dark-line-defects in GaAs/Si.

This indicates that high density of dislocations and the residual thermal stress is an important issue to obtain high-performance GaAs-based lasers on Si substrate, but not to GaN-based devices on sapphire. Recently, it was very interesting explanation of this question was reported from Nichia Chemical Industries, Ltd., [41] that the dislocations in GaN act as non-radiative recombination centers, but the carriers are prevented from reaching these defects due to extremely short diffusion length. This report may perverts the common sense of semiconductor researchers in GaAs/Si heteroepitaxial fields. It is only big luck that GaN devices work so well compared to GaAs-based devices on Si substrate.

1.2 Purpose of Dissertation

The successful launching of the GaN laser diodes by Nakamura and co-workers at Nichia Chemical Industries, Ltd., initiated enthusiastic activities in this field in the world. The recent progresses in crystal growth, conductivity control (p-type) and nitride-based laser diodes are prominet. On the contrary, the detailed fundametal physical mechanisms affecting laser active medium behavior, varous physical properties in GaN are under active investigation.

Up to now, from a physical view point, fundamental understanding or study has not fully achieved on the electron and hole transport properties, phonon characteristics, electronic properties and so on in GaN.

To catch up with the advances in GaN-based devices, the elimination of most of residual thermal stress, as well as further reduction of dislocation density introduced by the lattice mismatch, in GaAs layer grown on Si substrate is required for the development of long-lived LDs. The realization of high quality GaAs layer grown on Si substrate, the epoch-making approach to breakthrough the problems discussed in § 1.1 is demanded.

Considering above situations, two main purpose of this dissertation as listed below are set to investigate for future opto-electronic devices.

1) One of study sets out to investigate the fundamental mainly electrical and physical properties in GaN layer on sapphire substrate by means of the photoluminescence spectroscopy (PL), Micro–Raman scattering spectroscopy and the electron spin resonance (ESR) spectroscopy as well as theoretical calculations.

2) The other sets out to investigate the residual thermal stress in GaAs on Si substrate by introducing a New thin Si layer over porous Si substrate technology by means of the X-ray diffraction, the photoluminescence spectroscopy (PL), Micro–Raman scattering spectroscopy.

1.3 Organization of Dissertation

The dissertation is composed of six chapters and each of them is summarized as follows.

In **chapter 1**, the historical development and present status in GaN/sapphire and GaAs/Si and the necessity of these materials are reviewed. The problems faced in these materials are identifed and the purpose of this dissertation is described.

In **chapter 2**, the theoretical calculations of electron transport properties in both cubic and hexagonal phases of n-GaN, and hole transport property in cubic phase of p-GaN are perfomed. The overshoot effects of electron transporties in both cubic and hexagonal phases of GaN and GaAs are disscussed. In the hole transport calculations, the determination of valence band parameters, the anisotropy factors which determine hole mobilities and the temperature characteristics of hole mobilities are investigated. The mathematical representations of each scattering mechanisms are given briefly.

In **chapter 3**, Micro–Raman scattering by phonon-plasmon coupled mode in both *n*- and *p*-type GaN are disscussed. The Raman data are theoretically investigated and compared with the data measured by Van der Pauw Hall technique. The internal thermal stress reduction in post-patterned *n*-type GaN measured by Micro–Raman scattering is also discussed. The relationship between post-patterned area and thermal stress are shown.

In **chapter 4**, the nature of low-temperature electron spin resonance (ESR) signal from as-grown and 7 MeV high energy electron irradiated *n*-type GaN are discussed. The matrix elements coupling between Γ_1 conduction and Γ_6 valence and its conduction bands, and spin-orbit splitting of the Γ_6 are discussed using five-band $\mathbf{k}\cdot\mathbf{p}$ model. The detailed discussions of temperature dependences of ESR resonance intenisty and linewidth are presented.

To investigate the nature of broad emission band at 2.2 eV from *n*-tpe GaN, 7 MeV high energy electron irradiation is performd on *n*-type GaN and the results of ESR and optical induced ESR are discussed.

In **chapter 5**, the thermal stress relaxation in GaAs layer on new thin Si layer over porous Si substrate is discussed based on the results measured by the x-ray diffraction, low-temperature photoluminecesnce, Micro–Raman scattering. The data are compared to the conventional GaAs/Si.

In **chapter 6**, the conclusions drawn from this work are summarized.

Table 1.1: Important material parameters for GaN/sapphire and GaAs/Si heteroepitaxial systems.

Heteroepitaxial	Material	Crystal structure	Thermal expansion coefficient ($10^{-6}K^{-1}$)
GaN/Sapphire	GaN	Wurtzite	a=b : 5.59 c : 7.75
	Sapphire (α-Al_2O_3)	Corundum/ rhombohedral	a=b : 7.5 c : 8.5
GaAs/Si	GaAs	Zincblend	6.0
	Si	Diamond	2.4

Table 1.2: Band parameters and exciton binding energies of GaN and GaAs.

Material	Effective mass (m_0)		Spin-orbit splitting (meV)	Exciton binding energy (meV)
	Electron	Hole		
GaN[a)]	0.22	$m_{\perp}^{hh}$=1.65, $m_{\parallel}^{hh}$=1.1 $m_{\perp}^{lh}$=0.15, $m_{\parallel}^{lh}$=1.1	11	28
GaAs[b)]	0.068	m^{hh}=0.62 m^{lh}=0.074	340	5.3

[a)] References [6] and [42].
[b)] Reference [43].

Table 1.3: Covalent radius and electron negativity of the host atoms in III–V semiconductors.

Material	Covalent radius (nm)	Electron negativity
Ga	0.126	1.13
N	0.07	3.0
As	0.110	2.1

Reference [44].

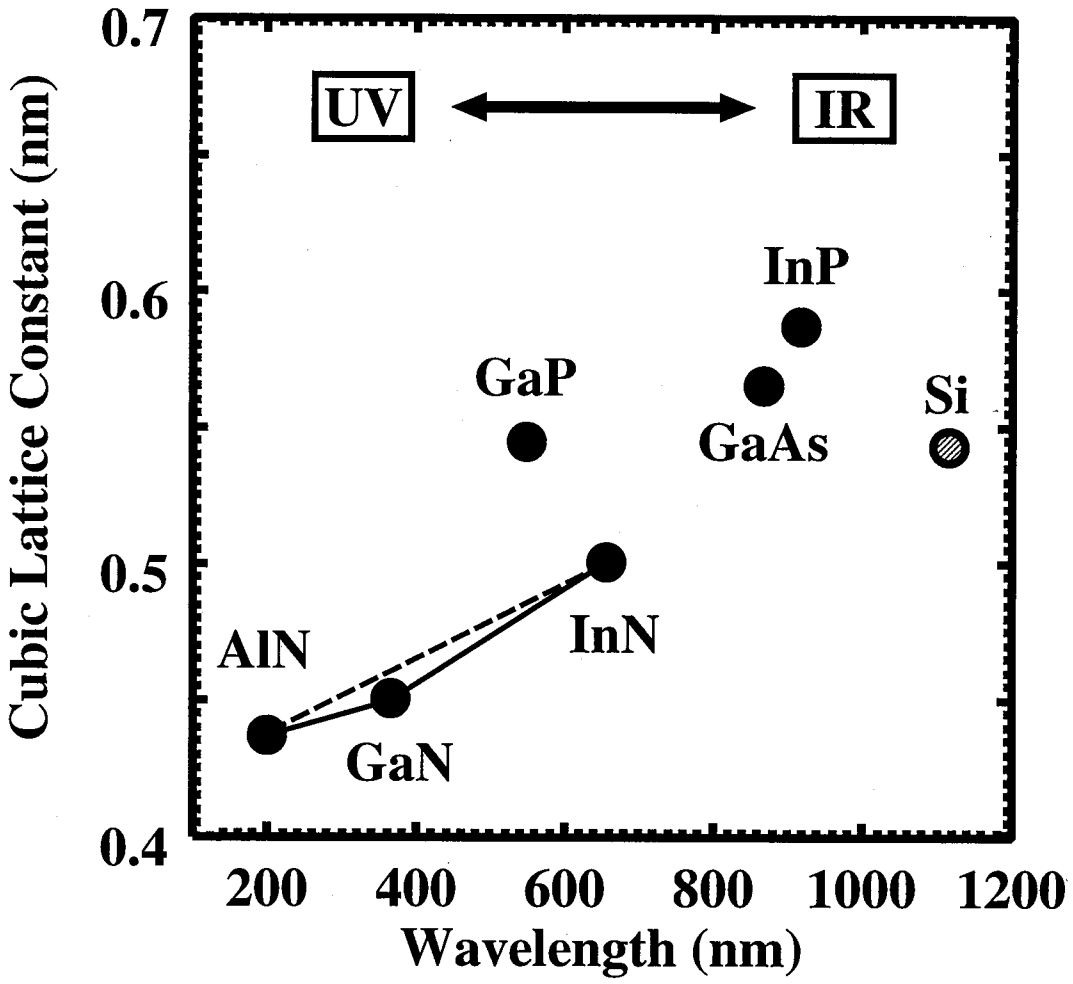

Figure 1.1: Relationship between lattice constants and wavelength corresponding to the bandgap energies of the III–V compounds. Lattice constants of nitrides are calculated assuming that each crystal forms a cubic lattice.

Bibliography

[1] H. P. Maruska and J. J. Tietjen: Appl. Phys. Lett. **65** (1969) 327.

[2] H. Amano, N. Sawaki, I. Akasaki and Y. Toyoda: Appl. Phys. Lett. **48** (1986) 353.

[3] H. Amano, M. Kito, K. Hiramatsu and I. Akasaki: Jpn. J. Appl. Phys. **28** (1989) L2112.

[4] S. Nakamura, N. Iwasa, M. Senoh and T. Mukai: Jpn. J. Appl. Phys. **31** (1992) 1258.

[5] H. Amano and I. Akasaki: Mat. Res. Soc. Ext. Abs. EA-21, (1990) 165.

[6] M. Suzuki and T. Uenoyama: J. Appl. Phys. **80** (1995) 6868.

[7] S .M Mohammad and H. Morkoç: Prog. Quantum Electron. **20** (1996) 361.

[8] Y. F. Wu. B. P. Keller, S. Keller, N. X. Nguyen, T. J. Jenkins, L. T. Kehias, D. P. Denbaars and U. K. Mishra: IEEE Electron Device Lett. **18** (1997) 438.

[9] M. Suzuki, T. Uenoyama and A. Yanase: Phys. Rev. B **52** (1995) 8132.

[10] J. Neugebauer and C. G. Van de Walle: Phys. Rev. B **50** (1994) 8067.

[11] R. Niebuhr, K. H. Bachem, U. Kaufmann, M. Maier, C. Merz, B. Santic, P. Schlotter and H. Jürgensen: J. Electron. Mter.**26** (1997) 1127.

[12] S. B. Zhang and J. E. Northrup: Phys. Rev. Lett. **67** (1991) 2339.

[13] D. B. Laks, C. G. Van de Walle, G. F. Neumark, P. E. Blóchl and S. P. Pantelides: Phys. Rev. B **45** (1992) 1096.

[14] S. W. Koch, H. Haug, G. Schmeider, W. Bohnert and C. Klingshirn: Phys. Status Solidi B **89** (1978) 431.

[15] W. W. Chow and S. W. Koch: Appl. Phys. Lett. **66** (1995) 3004.

[16] W. W. Chow, A. Knorr and S. W. Koch: Appl. Phys. Lett. **67** (1995) 754.

[17] G. Y. Zhao, G. Y. Yu, T. Egawa, J. Watanabe, T. Jimbo and M. Umeno: Appl. Phys. Lett. **71** (1997) 2424.

[18] L. Eckey, J. Holst, A. Hoffman, I. Broser, H. Amano, I. Akasaki, T. Detechprohm and K. Hiramatsu: J. Lumin. **72-74** (1998) 59.

[19] S. Nakamura, H. Senoh, N. Iwasa and S. Nagahama: Appl. Phys. **35** (1996) 1868.

[20] S. Nakamura, H. Senoh, N. Iwasa, S. Nagahama, T. Yamada and T. Mukai: Jpn. J. Appl. Phys. **34** (1995) L1332.

[21] M. Koike, N. Shibata, S. Ymasaki, S. Nagai, S. Asami, H. Kato, N. Koide, H. Amano and I. Akasaki: *Proc 1st int. Symp. GaN & Related Materials, Boston, 1995* (Material Research Society, Pittsburgh, 1995) Vol. 395, p 889.

[22] G. Landwehr: *Proc. 2nd. Int. Symp. Blue Laser and Light Emitting Diodes, Chiba, 1998* (Ohmsha, Tokyo, 1998) p. 3.

[23] M. Akiyama, Y. Kawarada and K. Kaminishi: J. Cryst. Growth. **68** (1984) 21.

[24] T. Soga, S. Hattroi, S. Sakai, M. Takeyasu and M. Umeno: Electron. Lett. **20** (1984) 916.

[25] S. F. Fang, K. Adomi, S. Iyer, H. Morkoç, H. Zabel, C. Choi and N. Otsuka: J. Appl. Phys. **68** (1990) R31.

[26] H. Okamoto, Y. Watanabe, Y. Kadota and Y. Ohmachi: Jpn. J. Appl. Phys. **26** (1987) L1950.

[27] R. W. Kaliski, C. R. Ito, D. G. Mclntyre, M. Feng, H. B. Kim, R. Bean, K. Zanio and K. C. Hsieh: J. Appl. Phys. **64** (1988) 1196.

[28] K. Ismail, F. Legoues, N. H. Karam, J. Carter and H. I. Smith: Appl. Phys. Lett. **59** (1991) 2418.

[29] N. Chand and S. N. G. Chu: Appl. Phys. Lett. **58** (1991) 74.

[30] S. Sakai, K. Kawasaki and N. Wada: Jpn. J. Appl. Phys. **29** (1990) L853.

[31] T. Soga, M. Yang, M. Umeno and T. Jimbo: Jpn. J. Appl. Phys. **35** (1996) 1401.

[32] T. Soga, T. Kato. M. Umeno and T. Jimbo: J. Appl. Phys. **79** (1996) 9375.

[33] R. Fischer, T. Henderson, J. Kim, W. T. Masselink, W. Kopp, H. Morkoç and C. W. Litton: Electron. Lett. **20** (1984) 945.

[34] R. Fischer, W. Kopp, J. Gedymin and H. Morkoç: Electron Devices **33** (1986) 1407.

[35] M. Askun, H. Morkoç, L. Lester, K. Duh, P. Smith, P. Chao, M. Longerbone and L. Erickson: Appl. Phys. Lett. **49** (1986) 1654.

[36] M. Yamaguchi and S. Kondo: Mat. Res. Soc. Symp. Proc. **145** (1989) 279.

[37] D. G. Depp, D. W. Nam, N. Holonyak, Jr., K. C. Hsien, R. J. Matyi, H. Shichijo, J. E. Epler and H. F. Chung: Appl. Phys. Lett. **51** (1987) 1271.

[38] R. Fischer, D. Neuman, H. Zabel, H. Morkoç, C. Choi and N. Otsuka: Appl. Phys. Lett. **48** (1986) 1223.

[39] J. W. Lee, H. Shichijio, H. L Tsai, and R. J. Matyi: Appl. Phys. Lett. **50** (1987) 31.

[40] M. Yamaguchi, A. Yamamoto, Y. Ithoh and C. Verie: Appl. Phys. Lett. **53** (1988) 2293.

[41] T. Mukai, H. Narimatsu and S.Nakamura: Jpn. J. Appl. Phys. **37** (1998) L839.

[42] R. Dingle, D. D. Sell, S. E. Stokowski and M. Ilegems: Phys. Rev. B **4** (1971) 1211.

[43] T. Ikoma and H. Ikoma: *Kagoubutu Handoutai no Kiso Bussei Nyumon* (Introduction to Fundamental Material Characteristics of Compund Semiconductors) (Baifukan, Tokyo, 1991) p. 14 [in Japapnese].

[44] J. C. Phillips: *Bonds and Bands in Semiconductors* (Academic, New York, 1973).

Chapter 2

Theoretical Studies on Transport Properties in Cubic Phase GaN

2.1 Introduction

It is well known that GaN film can be grown in either a hexagonal (wurtzite) or cubic (zincblende) structure, depending on the substrate symmetry and growth conditions, because of the small difference in the formation energy between these structures. Most of the work on GaN-related materials has focused on the hexagonal crystal phase. Cubic phase GaN is at present not experimentally characterized to the extent typical of hexagonal phase of GaN or more conventional semiconductors. However, theoretically, compared to hexagonal structures, cubic structures can possess superior electronic properties for device applications; for example, n- and p-type doping is known to be the most efficient what in other cubic III–V semiconductors [1], whereas doping in hexagonal phase of GaN has traditionally been recognized as being difficult, especially p-type doping. Furthermore, higher steady-state electron velocities are expected due to reduce phonon scattering in the higher crystallographic [2, 3, 4] and smaller effective masses.

Cubic-phase GaN was first reported by Seifert and Tempel [5]. Since then the number of studies on cubic phase-GaN has increased greatly. Unlike most of the other III–V semiconductors, because of the difficulties in growing a high-quality and single cubic phase rather than a hexagonal phase, very little is known about the material and physical properties of the cubic phase.

Several groups have reported the low field electron transport characteristics of hexagonal and cubic phases of n-GaN both experimentally and theoretically [6, 7, 8, 9, 10, 11, 12]. Only a few reported the high field electron transport and high temperature electron transport characteristics of cubic phase GaN [3, 13]. However, there is no report on hole transport properties of both cubic and hexagonal phases of GaN.

In this chapter, the theoretical characteristics of high field and high temperature electron transport in both cubic and hexagonal phases of GaN as well as GaAs by Monte Carlo simulation and the hole transport in cubic phases of GaN by relaxation time approximation will be discussed.

To the best of my knowledge, no theoretical investigation of the hole transport characteristics of the cubic phase of p-GaN that takes the Hall coefficient anisotropy factor into consideration has been reported yet. Moreover, there has been no report that considers all the relevant scattering mechanisms and the anisotropic bands in III–V cubic phase GaN simultaneously.

2.2 Fundamental Transport Theory

In the semiconductor crystal, vibrations of the ions from their equilibrium positions produce an instantaneous changes in the energy of electron a time-dependent component $H'(\boldsymbol{r})$ into the time-independent (adiabatic) one-electron Schrödinger equation. This interaction is the

electron-phonon interaction. It is usually weak enough for $H^{'}(\boldsymbol{r})$ to be regarded as a small perturbation ($H^{'}(\boldsymbol{r}) \ll H(\boldsymbol{r})$) which induces transitions between unperturbated states. This transition probability S from electron wave vectors $\boldsymbol{k}$ (initial) to $\boldsymbol{k}^{'}$ (final) is given by the familiar equation, so-called the *Fermi golden-rule* expression, of first order perturbation theory [14, 15],

$$S(\boldsymbol{k},\boldsymbol{k}^{'}) = \frac{2\pi}{\hbar}|\langle \boldsymbol{k}^{'}|H^{'}(\boldsymbol{r})|\boldsymbol{k}\rangle|^2 \delta\left(E_{\boldsymbol{k}^{'}} - E_{\boldsymbol{k}} \mp \hbar\omega\right). \tag{2.1}$$

The plus sign corresponds to the absorption of a phonon ($\hbar\omega$), and the minus sign, emission. (see Figs. 2.1(a) and 2.1(b)) The first-order perturbation theory does not give a delta function but a function of energy of the form $\sin(\xi t)/(\xi t)$, where t is the time and $\xi = 1/2\hbar \cdot (E_{\boldsymbol{k}^{'}} - E_{\boldsymbol{k}} \mp \hbar\omega)$, which approaches a delta function when $t \rightarrow \infty$.

It is now convenient to expand the scattering potential $H^{'}(\boldsymbol{r})$ in a Fourier series [16, 14, 15],

$$H^{'}(\boldsymbol{r}) = \sum_{q} H^{'}_{q} \exp(i\boldsymbol{q}\cdot\boldsymbol{r}), \tag{2.2}$$

where $\boldsymbol{q}$ is the phonon wave vector. The matrix element $|\langle \boldsymbol{k}^{'}|H^{'}(\boldsymbol{r})|\boldsymbol{k}\rangle|$ in eq. (2.1), which contains the momentum conservation, is given by [16, 14, 15]

$$\begin{aligned}
\langle \boldsymbol{k}^{'}|H^{'}(\boldsymbol{r})|\boldsymbol{k}\rangle &= \sum_{q} H^{'}_{q} \int_{\Omega} \mu^{*}_{\boldsymbol{k}^{'}}(\boldsymbol{r})\mu_{\boldsymbol{k}}(\boldsymbol{r}) \exp i(\boldsymbol{q} - \boldsymbol{k}^{'} + \boldsymbol{k})\cdot\boldsymbol{r} d\boldsymbol{r} \\
&= H^{'}_{q} I(\boldsymbol{k},\boldsymbol{k}^{'})\delta(\boldsymbol{q} + \boldsymbol{k} - \boldsymbol{k}^{'}) \\
&= H^{'}_{\boldsymbol{k}-\boldsymbol{k}^{'}} I(\boldsymbol{k},\boldsymbol{k}^{'}),
\end{aligned} \tag{2.3}$$

where $u_k(\boldsymbol{r})$ is the cell-periodic of the Bloch function and Ω is the crystal volume. Here $I(\boldsymbol{k},\boldsymbol{k}^{'})$, the "overlap integral" is defined by

$$I(\boldsymbol{k},\boldsymbol{k}^{'}) = \int u^{*}_{k^{'}}(\boldsymbol{r}) u_k(\boldsymbol{r}) d\boldsymbol{r}. \tag{2.4}$$

For electrons, whose wave functions are the s-like spherical symmetry in the conduction band, $I(\boldsymbol{k},\boldsymbol{k}^{'})$ is near unity. This fact reduces the complexity of the scattering terms in the electron transport properties. For holes within heavy- (hh) and light-hole (lh) bands, the wave functions exhibit a non-spherical symmetry due to its p-like symmetry. The $I(\boldsymbol{k}_i,\boldsymbol{k}^{'}_f)$ for GaN is assumed not to be strong function of wave vector $\boldsymbol{k}$ and can be approximated by the limit at $\boldsymbol{k} = 0$, where the admixture of s- and p-like symmetries vanishes. A hole is scattered from the initial state $\boldsymbol{k}$, in band i ($\boldsymbol{k}_i$) to the final state $\boldsymbol{k}^{'}$, in band f ($\boldsymbol{k}^{'}_f$), $I(\boldsymbol{k}_i,\boldsymbol{k}^{'}_f)$ is reduced to [17]

$$I(\boldsymbol{k}_i,\boldsymbol{k}^{'}_f) = \begin{cases} (1+3\cos^2\theta)/4, & \text{for } i = f : \text{intra-band} \\ 3(1-\cos^2\theta)/4, & \text{for } i \neq f : \text{inter-band} \end{cases}, \tag{2.5}$$

where θ is the angle between $\boldsymbol{k}_i$ and $\boldsymbol{k}^{'}_f$.

Using eq. (2.1) it is straightforward to find the scattering rate $W(\boldsymbol{k})$ by summing $S(\boldsymbol{k},\boldsymbol{k}^{'})$ over all states $\boldsymbol{k}^{'}$ given by [16, 14, 15]

$$\begin{aligned}
W(\boldsymbol{k}) &= \frac{\Omega}{(2\pi)^3}\int_{\Omega} S(\boldsymbol{k},\boldsymbol{k}^{'}) d\boldsymbol{k}^{'} \\
&= \frac{2\pi}{\hbar}\frac{\Omega}{(2\pi)^3}\int_{\Omega} |\langle \boldsymbol{k}^{'}|H^{'}|\boldsymbol{k}\rangle|^2 \delta\left(E_{\boldsymbol{k}^{'}} - E_{\boldsymbol{k}} \mp \hbar\omega\right) d\boldsymbol{k}^{'} \\
&= \frac{\Omega}{(2\pi)^3}\int_0^{2\pi}\int_0^{\pi}\int_0^{\infty} S(\boldsymbol{k},\boldsymbol{k}^{'}) k^{'2} \sin\theta dk^{'} d\theta d\phi.
\end{aligned} \tag{2.6}$$

The last term is the expression at a spherical coordinate system with the $\boldsymbol{k}$ direction as the polar axis and θ is the polar angle (angle between $\boldsymbol{k}$ and $\boldsymbol{k}^{'}$) and ϕ is the azimuthal angle. $S(\boldsymbol{k},\boldsymbol{k}^{'})$

does not depend on ϕ due to symmetry, the integration over the ϕ can be done immediately, yielding 2π. On the other hand, the integration over the θ and k' can not be done independently because it contains both the energy and momentum conservation conditions. The details of this integration will be discussed in each scattering mechanisms.

In the Monte Carlo simulation it is necessary to calculate $W(\boldsymbol{k})$ and determine the final-state $\boldsymbol{k}'$ including the angle distribution of the scattering.

2.3 Electron Transport Characteristics Calculated by Monte Carlo Simulation

The scattering mechanisms included in the calculations are deformation potential by acoustic and optical phonons, polar optical phonon, ionized impurity and inter-valley (three valleys) deformation potential.

2.3.1 Scattering mechanisms : electron transport

The theories for the scattering mechanisms in the electron transport analysis are summarized briefly. The final form of scattering rates derived in each scattering mechanisms are included into Monte Carlo program. The Monte Carlo method is often used in novel device simulations owing to its inherent flexibility and the relative ease with which basic underlying physical effects can be incorporated into the model.

Density of State: The electron effective density of states of a given spin $N(E_k)$ per unit energy in the band is given by [16]

$$N(E_k) = \frac{(2m^*)^{3/2}}{4\pi^2\hbar^3}\sqrt{E_k}, \tag{2.7}$$

where m^* is the electron effective mass used in this study as shown in Table 2.2. and E_k is the energy band which is discussed in Appendix A. $N(E_k)$ is used in the following discussion about scattering mechanisms.

Acoustic mode deformation potential scattering: One of the most common phonon scattering process is the interactions with the acoustic modes of the lattice through a deformation potential. A long-wavelength acoustic wave moving through the lattice causes a local strain in the crystal which perturbs the energy band. This change in the bands produces a weak scattering potential, which leads to being able to express the perturbing potential as [16, 14, 15],

$$H' = E_1\Delta = E_1\nabla\cdot\boldsymbol{u}(\boldsymbol{r}.t), \tag{2.8}$$

where E_1 is the deformation potential and Δ is the dilation of the lattice produced by a wave whose Fourier coefficient is $\boldsymbol{u}(\boldsymbol{r}.t)$. $\boldsymbol{u}(\boldsymbol{r}.t)$ is written as

$$\boldsymbol{u}(\boldsymbol{r}.t) = \sum_q \left(\frac{\hbar}{2\rho\Omega\omega_q}\right)^{1/2} \boldsymbol{e}_q \left(a_q + a_{-q}^{\dagger}\right) e^{i\boldsymbol{q}\cdot\boldsymbol{r}}, \tag{2.9}$$

where $\boldsymbol{e}_q$ is the polarization unit vector, ρ is the density of material, and a_q and $a_{-q}^{\dagger}$ are the annihilation and creation operations, respectively. Note that $\boldsymbol{e}_q\cdot\boldsymbol{q}$ is zero for transverse and $\boldsymbol{e}_q\cdot\boldsymbol{q}$ is $\boldsymbol{q}$ for longitudinal modes. By applying eq. (2.1) using eq. (2.8) and eq. (2.9) leads to

$$\begin{aligned} S_{ac}(\boldsymbol{k},\boldsymbol{k}') &= \frac{\pi E_1^2 q^2}{\rho\omega_q\Omega}\left(n_q + \frac{1}{2} \mp \frac{1}{2}\right) \times \delta\left(\boldsymbol{k}' - \boldsymbol{k} \mp \boldsymbol{q}\right)\delta\left(E_{\boldsymbol{k}'} - E_{\boldsymbol{k}} \mp \hbar\omega_q\right) \\ &= \frac{\pi E_1^2 q^2}{\rho\omega_q\Omega}\left(n_q + \frac{1}{2} \mp \frac{1}{2}\right) \times \delta\left(\frac{\hbar^2 q^2}{2m^*} \pm \frac{\hbar^2 k q\cos\theta'}{m^*} \mp \hbar\omega_q\right), \end{aligned} \tag{2.10}$$

where n_q is the Bose-Einstein distribution and θ' is the angle between $\boldsymbol{k}$ and $\boldsymbol{q}$. Scattering processes in which the phonon energy may be ignored are termed *elastic scattering events*. For most practical cases the acoustic mode energies are much lower than the thermal energy except the lower temperatures and thus the Bose-Einstein distribution can be expressed under the *equipartition approximation* as $N_q \approx k_b T/\hbar\omega_q \gg 1$. Since this distribution is so large and the energy exchange is so small, it is quite easy to add the two terms for emission and absorption of phonons. For electron in a simple, spherical energy surface and parabolic bands, the final form of scattering rate by summing eq. (2.10) over all states $\boldsymbol{k}'$ leads to

$$W_{ac}(\boldsymbol{k}) = \frac{2\pi E_1 k_b T}{\hbar C_L} N(E_k), \tag{2.11}$$

where $N(E_k)$ is the density of state defined by eq. (2.7).

Nonpolar optical mode scattering: The matrix element given by eq. (2.4) in nonpolar optical phonon scattering is found from a deformable ion model, in which the two sublattices move relative to one another. Thus the potential field of each ion is displaced slightly. This causes a resulting shift in the bond charges and produces a macroscopic deformation field D_0. This field is zero-order process, in that the resulting interaction potential is independent of the wave vector, as [16, 14, 15]

$$H' = \boldsymbol{D}_0 \boldsymbol{u}(\boldsymbol{r}.t), \tag{2.12}$$

where $\boldsymbol{u}(\boldsymbol{r}.\mathrm{t})$ is the Fourier coefficient given by eq. (2.9). By applying eq. (2.1) using eq. (2.12) and eq. (2.9) leads to

$$S_{npop}(\boldsymbol{k}, \boldsymbol{k}') = \frac{\pi D_0^2}{\rho\omega_0\Omega}\left(n_0 + \frac{1}{2} \mp \frac{1}{2}\right) \times \delta\left(\boldsymbol{k}' - \boldsymbol{k} \mp \boldsymbol{q}\right) \delta\left(E_{\boldsymbol{k}'} - E_{\boldsymbol{k}} \mp \hbar\omega_0\right). \tag{2.13}$$

In this equation, the approximation of $\omega_q = \omega_0$ and $n_q = n_0$ are applied since the dispersion relation for the nonpolar optical modes is quite flat or with very little dependence on the magnitude of the wave vector $\boldsymbol{q}$. Nonpolar optical phonon can occur not only within a single minimum (or valley) of band but intervalley or interband scatterings. For intervalley phonon scattering, the dominant part of phonon wave vector is quite large, so that no significant error is made by continuing to treat the frequency of the optical phonon as a constant. Combining the various constants using eq. (2.13) and eq. (2.1) gives the simple scattering rate of

$$\begin{aligned} W_{npop}(\boldsymbol{k}) &= \frac{\pi D_{ij} Z_j}{\rho\omega_{ij}}\left(n(\omega_{ij}) + \frac{1}{2} \mp \frac{1}{2}\right) N(E_k \pm \hbar\omega_{ij} - \Delta E_{ij}) \\ &= \frac{\pi D_0}{\rho\omega_0}\left(n(\omega_0) + \frac{1}{2} \mp \frac{1}{2}\right) N(E_k \pm \hbar\omega_0), \end{aligned} \tag{2.14}$$

where i and j are the i- and j-th bands, D_{ij} is the intervalley macroscopic deformation field, Z_j is the number of equivalent valley, ΔE_{ij} is the energy difference between i-th and j-th bands and $N(E_k \pm \hbar\omega_{ij} - \Delta E_{ij})$ and $N(E_k \pm \hbar\omega_0)$ are the densities of state at final state which can be calculated by eq. (2.7).

Polar optical mode scattering: In polar materials the vibrations of oppositely charged atoms give rise to long-wave macroscopic electric field in addition to deformation potentials, and the interaction of the electron with these fields produces additional components of scattering. The polar scattering is a very effective scattering mechanism for electrons in the central valley of the group III–V and II–VI semiconductors. Also it can be effective for holes.

The displacement of the two atoms gives the details of the polarization dipoles $\boldsymbol{P}$, and the electric flux density $\boldsymbol{D} = \varepsilon_0 \boldsymbol{E} + \boldsymbol{P}_{ion} + \boldsymbol{P}$, where $\boldsymbol{E}$ is the electromagnetic field and $\boldsymbol{P}_{ion}$ is the polarization dipoles of atoms itself. The $\boldsymbol{P}$ is expressed by $(e^* N/\Omega)\boldsymbol{u}$, where $e*$ is the *magnitude of effective charge* on the atoms, N is the number of pairs of ions and $\boldsymbol{u}$ is the

relative displacement between two ions. On the other hand, $\boldsymbol{P}_{ion}$ has the relationship with $\boldsymbol{E}$ as $\varepsilon_\infty \boldsymbol{E} = \varepsilon_0 \boldsymbol{E} + \boldsymbol{P}_{ion}$. Thus the electric flux density $\boldsymbol{D}$ is given by

$$\boldsymbol{D} = \varepsilon_\infty \boldsymbol{E} + \frac{e^* N}{\Omega} \boldsymbol{u}, \tag{2.15}$$

with

$$e^* = \left(\frac{\Omega M}{N}\right)^{1/2} \omega_0 \varepsilon_\infty \left(\frac{1}{\varepsilon_p}\right)^{1/2}, \tag{2.16}$$

where $1/\varepsilon_p$ is given in terms of the static (ε_s) and high-frequency (ε_∞) dielectric constants ($1/\varepsilon_p = 1/\varepsilon_s - 1/\varepsilon_\infty$) and M is the reduced mass. Now the potential $U(r)$ is found by integrating the electromagnetic field $\boldsymbol{E}$ derived from eq. (2.15) over the position vector $\boldsymbol{r}$. The polar scattering potential $H^{'}$ is given by [16, 14, 15]

$$\begin{aligned} H^{'} &= -eU(\boldsymbol{r}) \\ &= \sum_q i \frac{e}{q} \left(\frac{\hbar\omega_0}{2\varepsilon_p \Omega}\right)^{1/2} \left(a_q + a_{-q}^{\dagger}\right) e^{i q \cdot r}. \end{aligned} \tag{2.17}$$

The transition probability can be obtained from eq. (2.1) with eq. (2.17) and is given by

$$S_{pop}(\boldsymbol{k}, \boldsymbol{k}^{'}) = \frac{\pi e^2 \omega_0}{\varepsilon_p \Omega} \left(n(\omega_0) + \frac{1}{2} \mp \frac{1}{2}\right) \times \delta\left(\boldsymbol{k}^{'} - \boldsymbol{k} \mp \boldsymbol{q}\right) \delta\left(E_{\boldsymbol{k}^{'}} - E_{\boldsymbol{k}} \mp \hbar\omega_0\right), \tag{2.18}$$

so that the result for the scattering rate is given by

$$W_{pop}(\boldsymbol{k}) = \frac{e^2 \omega_0}{8\pi\varepsilon_p} \frac{k}{E_k} \left(n(\omega_0) + \frac{1}{2} \mp \frac{1}{2}\right) \ln\left(\frac{q_{max}}{q_{min}}\right), \tag{2.19}$$

where

$$\left.\begin{aligned} q_{min} &= k\left|1 - \sqrt{1 \pm \tfrac{\hbar\omega_0}{E_k}}\right| \\ q_{max} &= k\left|1 + \sqrt{1 \pm \tfrac{\hbar\omega_0}{E_k}}\right| \end{aligned}\right\}. \tag{2.20}$$

Nonphonon Scattering: Ionized Impurity Scattering: There are several scattering mechanisms which do not involve direct interaction between the phonons and the electron. Here the scattering by ionized impurity atoms will also be discussed. The electron scattering from the Coulomb potential of an ionized impurity atom, it is necessary to consider the long-range nature of the potential. A screening of the Coulomb potential by the free carriers was invoked to treat the long-range potential. For the spherical symmetry about the scattering center, or ion location, the potential is screened in a manner that give rise to a standard screened Coulomb form [16, 14, 15] as

$$V(r) = \frac{Ze}{4\pi\varepsilon_s r} \exp(-q_D r), \tag{2.21}$$

where Z is the the level of ionization of the impurity atom and q_D is the reciprocal of the Debye screening length which is given by

$$q_D^2 = \frac{e^2 n_0}{\varepsilon_s k_B T}. \tag{2.22}$$

The scattering potential $H^{'}$ is written by

$$H^{'} = eV(r) = \frac{Ze^2}{4\pi\varepsilon_s r} \exp(-q_D r). \tag{2.23}$$

The transition probability of ionized impurity scattering at impurity concentration N_I can be obtained from eq. (2.1) with eq. (2.23) and is given

$$S_{ion}(\boldsymbol{k}, \boldsymbol{k}^{'}) = \frac{2\pi}{\hbar} \frac{N_I Z^2 e^4}{\Omega \varepsilon_s^2} \frac{\delta(E_{k'} - E_k)}{(q^2 + q_D^2)^2}, \tag{2.24}$$

where $q^2 = \left(\boldsymbol{k}' - \boldsymbol{k}\right)^2 = 2k^2(1-\cos\theta)$, θ is the angle between $\boldsymbol{k}'$ and $\boldsymbol{k}$. The final form of scattering rate by summing eq. (2.24) over all states $\boldsymbol{k}'$ leads

$$W_{ion}(\boldsymbol{k}) = \frac{\pi N_I Z^2 e^4 N(E_k)}{\hbar\varepsilon_s^2}\int_0^{\pi}\frac{\sin\theta d\theta}{\{2k^2(1-\cos\theta)+q_D^2\}^2} = \frac{2\pi N_I Z^2 e^4 N(E_k)}{\hbar\varepsilon_s^2}\frac{1}{q_D^2(4k^2+q_D^2)}, \tag{2.25}$$

where $N(E_k)$ is the density of state defined in eq. (2.7).

2.3.2 Determination of final states after scattering

The choice of the electron state (final state) as well as the magnitude of electron wave vector $\boldsymbol{k}'$ after scattering are necessary to perform the Monte Carlo analysis [16] for the transport properties using above mentioned scattering mechanisms. The magnitude of electron wave vector $\boldsymbol{k}'$ after scattering is readily obtained by the energy conservation law.

In case of the isotropic scattering such as acoustic phonon scattering any state $\boldsymbol{k}'$ belonging to the energy conserving sphere has the same probability of the occurrence, independently of the angle formed with the initial state $\boldsymbol{k}$. The probability $P(\phi', \theta')$ that the polar angles of $\boldsymbol{k}'$ with respect to any convenient directions will be contained in the intervals $d\theta'$ and $d\phi'$ is given by $P(\phi', \theta')d\phi' d\theta'$, and $P(\phi', \theta') = \sin\theta'$ because of the isotropic character of the scattering. Thus ϕ' and θ' can be expressed using two random numbers r_1 and r_2 generated between 0 and 1 as

$$\left.\begin{array}{ll} \phi' & = 2\pi r_1 \\ \cos\theta' & = 1 - 2r_2 \end{array}\right\}. \tag{2.26}$$

Thus the final state of $\boldsymbol{k}' = (k_x', k_y', k_z')$ is expressed by

$$\left.\begin{array}{ll} k_x' & = k'\sin\theta'\cos\phi' \\ k_y' & = k'\sin\theta'\sin\phi' \\ k_z' & = k'\cos\theta' \end{array}\right\}. \tag{2.27}$$

When this simple model is used, the polar axis is usually taken along the direction of the applied field.

On the other hand, the nonisotropic scattering such as polar optical phonon scattering or ionized ion scattering, the determination of $\boldsymbol{k}'$ is a little complicated. The transition probability is incident of the azimuthal angle ϕ of $\boldsymbol{k}'$ around $\boldsymbol{k}$ and the angle ϕ is again chosen at random according to eq. (2.26) as $\phi = 2\pi r_3$, where r_3 is the random number. The angle θ between initial and final states is deduced from $r_4 = W(\theta)/W(\boldsymbol{k})$ (for example, see the second and third terms in eq. (2.25), where r is the random number generated between 0 and 1, as

$$\cos\theta = 1 - \frac{2r_4}{1+(1-r_4)\left(\frac{2k}{q_D}\right)^2}, \tag{2.28}$$

where q_D is the reciprocal of the Debye screening length defined in eq. (2.22) and r_4 is the random number.

Now the new coordinate system (k_x^r, k_y^r, k_z^r) is introduced to determine $\boldsymbol{k}'$, where the $\boldsymbol{k}$ is taken to be the principle axis using the rotation angles α and β as shown in Fig. 2.1(c). Figure 2.1(d) shows the relationship between $\boldsymbol{k}$ and $\boldsymbol{k}'$ in terms of ϕ and θ. Thus the $\boldsymbol{k}'$ is expressed as

$$(k'\sin\theta\cos\phi, k'\sin\theta\sin\phi, k'\cos\theta) \tag{2.29}$$

in the (k_x^r, k_y^r, k_z^r) system. If the component of $\boldsymbol{k}'$ is to determine with respect to k_x, k_y and k_z, the following transfer matrix can be used:

$$\begin{pmatrix} \cos\beta & \cos\alpha\sin\beta & \sin\alpha\sin\beta \\ -\sin\beta & \cos\alpha\cos\beta & \sin\alpha\cos\beta \\ 0 & -\sin\alpha & \cos\alpha \end{pmatrix}, \tag{2.30}$$

where $\sin\alpha$, $\sin\beta$, $\cos\alpha$ and $\cos\beta$ are expressed as

$$\left.\begin{array}{ll} \sin\alpha = \frac{\sqrt{k_x^2+k_y^2}}{k}, & \cos\alpha = \frac{k_z}{k} \\ \sin\beta = \frac{k_x}{\sqrt{k_x^2+k_y^2}}, & \cos\beta = \frac{k_y}{\sqrt{k_x^2+k_y^2}} \end{array}\right\}. \tag{2.31}$$

By collecting eqs. (2.29), (2.30) and 2.31 the final state of $\boldsymbol{k}'$ is obtained by

$$\begin{pmatrix} k_x' \\ k_y' \\ k_z \end{pmatrix} = \begin{pmatrix} \frac{k_y}{\sqrt{k_x^2+k_y^2}} & \frac{k_x k_y}{k\sqrt{k_x^2+k_y^2}} & \frac{k_x}{k} \\ \frac{-k_x}{\sqrt{k_x^2+k_y^2}} & \frac{k_y k_z}{k\sqrt{k_x^2+k_y^2}} & \frac{k_y}{k} \\ 0 & \frac{-\sqrt{k_x^2+k_y^2}}{k} & \frac{k_z}{k} \end{pmatrix} \begin{pmatrix} k' \sin\theta\cos\phi \\ k' \sin\theta\sin\phi \\ k' \cos\theta \end{pmatrix}. \tag{2.32}$$

2.3.3 Results: electron transport characteristics

To perform the calculation of electron transport characteristics, the many particles Monte Carlo program which considers a three valley model with nonparabolicity based on the scattering mechanisms and estimation of electron state (final state) as mentioned § 2.3.1 and § 2.3.2 was developed. Recent calculations have demonstrated the importance of including the satellite valleys in Monte Carlo simulations the steady state drift velocity field relation in bulk GaN at temperature as high as 300 K [8, 18]. The Monte Carlo technique, employed in this study, to treat electron transport is based on the technique described in the excellent reviews by Tomizawa [16], Jacoboni and Reggiani [19], Lugi and Ferry [20], and Fischetti and Laux [21].

The material parameters of cubic phase of GaAs, cubic phase of GaN and hexagonal phase of GaN used are summarized in Table 2.1. The parameters for the valleys are estimated from recent band structure calculations [22] and are given in Table 2.2.

A variety of field strength are simulated to understand the effect on the transient behavior of the electron. The donor concentration is set to 1×10^{17} cm^{-3} and degeneracy effects are not incorporated. In each simulation, 4000 electrons are initially distributed in the sample according to an equilibrium Maxwellian distribution at 300 K. Number of electrons larger than 10000 were tried to check the results of velocity characteristics, and no significant difference were found in the results between 4000 and 10000 electrons. The simulation steps the electric field from zero to full intensity at the beginning of the run ($t = 0$), after which the velocity of electrons is averaged at 5 fs intervals. This interval time was also checked to know the effect on the velocity characteristics. The average distance traveled as function of time found by integrating the drift velocity.

The electron velocity versus distance for GaAs and for cubic and hexagonal phases of GaN are shown in Figs. 2.1(a), 2.1(b) and 2.1(c). All three materials overshoot only occurs at field strength larger than the peak steady state velocity field. Also the fields which produce the highest steady state velocities (150 kV/cm in hexagonal GaN and 120 kV/cm in the cubic GaN) are very close to the results using the full band Monte Carlo calculations reported by Kolnik *et al.* [22].

Comparing the two phases of GaN the cubic phase have an advantage because of its higher steady state velocity. However, Figs. 2.2(a) and 2.2(b) in the deep submicron region, where the overshoot effects are important, indicate that nearly equal performance of submicron device may be obtained.

The electron transit time as a function of distance traveled is shown in Fig. 2.3. The field chosen minimize the electron transit time at 1 μm. Using relation

$$f_T = \frac{1}{2\pi\tau}, \tag{2.33}$$

where τ is the transit time at distance 1 μm, the cutoff frequencies which are the good estimation for maximum operating frequency of field effect transistor (FET) were determined. In case of GaAs, τ as 4.5 ps is determined and the corresponding cutoff frequency is estimated to be 35 GHz. Values as high as 20 GHz have been measured in 1 μm modern GaAs modulation doped field effect transistors, not so far from the upper limit predicted from eq. (2.33) alone. The values determined as 2.7 and 3.0 ps for cubic and hexagonal phases of GaN suggest that the maximum operating frequency may be capable of achieving a f_T as high as 50 GHz in 1 μm GaN FETs. A slightly lower field strength is needed to achieve as high as 50 GHz for a cubic phase of GaN FETs. However, the drain bias at 50 GHz operation requires much higher than that of GaAs. For the microwave power FETs, a high current-gain cut-off frequency (f_T) along with a high saturation current is of essential importance.

The transit time as a function of distance in the overshoot regime is shown in Fig. 2.4. The applied fields were chosen to minimize the transit time across a 0.1 μm region. Generally, it is expected that the electrons with small effective mass (m^*) have greater acceleration due to electric field, and thus have greater velocity and a short transit time. In case of this study, effective masses of both cubic and hexagonal are grater than that of GaAs. Thus the higher velocity is estimated in GaAs rather than GaN. However, because of larger effective mass of GaN its ability to operate at higher voltages allows the transit time to be reduced below that of GaAs. From the view pint of this estimation, the electric property of GaAs shows inferior to that of GaN in the device with distance below 0.2 μm due to higher velocity, where velocity overshoot is very important in high speed devices.

The peak transit time as a function of applied electric fields is shown in Fig. 2.5. In the calculation range, the drift velocities increase with increase in applied electric field and show no saturation behavior in both cubic and hexagonal phases. This may be due to neglecting the impact ionization effect like Keldysh formula [23]. In comparison with the hexagonal phase GaN, the cubic phase GaN possesses a remarkable advantage in velocity characteristic especially at high electric field.

The peak transit time as a function of temperature at electric field of 300 kV/cm and 600 kV/cm is shown in Fig. 2.6. The same temperature characteristic of velocity is shown in both phases, however, the higher velocity is obtained from cubic phase GaN compared to hexagonal phase GaN.

2.4 Hole Transport Characteristics Calculated by Relaxation Time Approximation

2.4.1 Outline of hole transport calculations

In this section, the Hall coefficients anisotropy factors (r_A) for cubic phase of GaN are determined and theoretical hole transport characteristics (Hall and drift mobilities, and effective Hall factor) are calculated. Also the extent to which r_A differs from unity for valence bands is investigated, and the temperature dependence of the Hall and drift mobilities and the effective Hall factors are discussed.

The scattering mechanisms included in the calculations are deformation potential by acoustic and optical phonons, polar optical phonon, piezoelectric, ionized impurity and interband deformation potentials between heavy- and light-hole scattering. The interband deformation potential scattering, especially from the light-hole to the heavy-hole band, is the most important scattering in the high temperature regime [17]. The screening effects for the phonon scattering mechanism are neglected, because the low-impurity concentrations are considered here. All scattering rates in this study have been derived assuming a nonparabolic [24], which is given in Appendix A, spherical bands, and band warping is accounted for through the use of approximate overlap functions as discussed in § 2.2. This method enables one to calculate the Hall and drift mobilities and the effective Hall factor of hole bands separately.

The calculated hole transport characteristics, with changing compensation ratio over a wide range of temperatures (T=50 - 400 K), are based on the "relaxation time approximation" or "Mathiessen's rule", assuming transport in both heavy-hole and light-hole bands (a two-band model) with scattering allowed between the bands.

The spin-orbit splitting energy at the top of the valence band (Δ_{so}) is neglected in this calculations because there are no experimental measurements nor theoretical calculation for cubic-phase GaN. It has been reported that the value of Δ_{so} of hexagonal and cubic structures are very close to each other for many other semiconductors. Applying this assumption also to GaN case, the Δ_{so} value of the cubic-phase is estimated to be 11 - 30 meV from that of the hexagonal-phase [25, 26], which is one order of magnitude smaller compared to other III–V compound semiconductors such as GaAs (Δ_{so} = 340 meV). The hole occupation probability in the split-off hole bands is low in the low temperature regime, and thus it may not greatly affect the hole transport characteristics. Thus the calculated data addressed in this chapter are highly reliable. However, it should be noted that neglecting the split-off holes results in an over-estimation of hole mobility in the high temperature regime ($\geq$ 300 K).

2.4.2 Valence band anisotropy parameters

In general, the cubic III–V semiconductors exhibit considerably warped of surfaces that have numerous interesting consequences for hole transport. At most, calculations yield a drift mobility, whereas the experimental measured quantity is usually the Hall mobility. The two mobilities are related by a known Hall coefficient factor. For the nondegenerate spherical symmetric bands, the Hall coefficient factor can be written as

$$r_i = \frac{\langle \tau_i^2 \rangle}{\langle \tau_i \rangle^2}, \tag{2.34}$$

where τ is the carrier scattering time, $\langle \cdots \rangle$ indicates a thermal average over the distribution of carrier energy and the index i refers to heavy ($i = 1$) and light ($i = 2$) holes.

When the bands are warped, the Hall coefficient factor depends on the degree of warping as well as the scattering mechanism, and can be written as

$$r_i = r_{Ai} \frac{\langle \tau_i^2 \rangle}{\langle \tau_i \rangle^2}, \tag{2.35}$$

where r_{Ai} is the anisotropy factor for i-th hole band.

Prior to calculating r_{Ai}, it is necessary to determine the valence band parameters L, M and N defined in terms of the interband matrix element [27]. Then A, B and C parameters, which have been used in an approximate expression for the light- and heavy-hole energy surfaces given by Dresselhaus *et al.*, [28] were determined. These valence band parameters were calculated from those of Luttinger effective mass parameters recently reported by Fan *et al.* [25] According to them, the Luttinger parameters are $\gamma_1 = 3.07$, $\gamma_2 = 0.86$ and $\gamma_3 = 1.26$. The notations for L, M and N are the same those as shown in ref. [27]. Within the five-band $\mathbf{k}\cdot\mathbf{p}$ model, the Luttinger valence band parameters are given by

$$\begin{aligned}
\gamma_1 &= -\frac{1}{3}(F + 2G + 2H_1 + 2H_2) - 1 + \frac{1}{2}q, \\
\gamma_2 &= -\frac{1}{6}(F - 2G - H_1 - H_2) - \frac{1}{2}q, \\
\gamma_3 &= -\frac{1}{6}(F - G + H_1 - H_2) + \frac{1}{2}q,
\end{aligned} \tag{2.36}$$

where F, G, H_1 and H_2 are constants defined by Dresselhaus, kip and Kittel (DKK) [28]. In the DKK model, H_1 and F are derived from the interactions between Γ_{15} and Γ_2' states. G and H_2 are derived from the Γ_{12}' states and the Γ_{25} states, respectively. q is the correction term and is always very small.

In order to calculate r_{Ai}, the Lax and Mavroides [29], Beer [30] and Strin [31] formulae expressed in ref. [27] were used. According to their expressions, r_{Ai} is given by

$$r_{Ai} = \frac{a_d a_{12}}{a_{11}^2}, \tag{2.37}$$

where a_d, a_{12} and a_{11} are in terms of Γ. The detailed descriptions of a_d, a_{12} , a_{11} and Γ are given in Appendix B. The used valence band parameters related to the equations are given in Table 2.3.

2.4.3 Scattering mechanisms: hole transport

The theories for the scattering mechanisms in the hole transport analysis are summarized briefly. It should be noted that the basic treatments of the scattering mechanisms are the same as those discussed in § 2.3.1. Here, only the scattering due to the ionized impurity and nonpolar optical mode will be discussed.

Ionized impurity scattering: In this chapter the ionized impurity scattering mechanism for hole bands can be treated using the Brooks-Herring approximation [32], where particles interact via the screened Coulombic potential.

For a low hole concentration (nondegenerate case) and high temperatures, the inverse of screening length λ_D, can be written as

$$\frac{1}{\lambda_D^2} = \frac{e^2}{\varepsilon_s k_B T}\{p + (p + N_D)[1 - (N_D + p)/N_A]\}, \tag{2.38}$$

where e is the electron charge, p is the total hole concentration, N_A and N_D is the concentration of acceptors and donors, respectively, ε_s is the static dielectric constant, k_B is Boltzmann's constant and T is the temperature. p was calculated using the charge neutrality equation given by

$$\frac{p(p + N_D)}{N_A - N_D - p} = \frac{N_v}{g_i} \exp\left(-\frac{\Delta E_a}{k_B T}\right), \tag{2.39}$$

where N_v is the effective density of states in the valence band, ΔE_a ($\Delta E_a = E_a - E_v$) is the acceptor activation energy, and g_i is the spin degeneracy factor, which is 4 in this case. The value of E_a is still argued area in both experimentally and theoretically. In the case of the commonly used Mg acceptor for p-type GaN, the activation energy in the range from 150 to 250 meV is higher than that estimated by the ideal acceptor hydrogenic model which might yield the correct order of magnitude of true ionization energy. (Using an acceptor effective mass of $0.76m_0$ and low-frequency dielectric constant of 9.5 results in E_a is determined $\approx$ 115 meV.) The origin of the high acceptor activation energy is still far from understood. These high values imply that at room temperature, the hole concentration is less than 1 percent of the Mg concentration. The difference between the experimental and calculated values of the activation energy is not negligible; however, it should be noted that the activation energy found experimentally is close to that determined using this ideal model [33]. E_a used in this study is 120 or 250 meV.

The Coulombic scattering rate due to the density of ionized impurities N_I ($N_I = p + 2N_D$) and the level of ionization of the impurity atom Z_I is given by [17, 34]

$$S_{ion}(\boldsymbol{k}_i, \boldsymbol{k}_f') = \frac{Z_I^2 N_I e^4 m_f^*}{8\pi\epsilon_s^2 \hbar^3} \frac{1}{k_i^3} \int_{-1}^{1} \frac{(1-y)G(y)}{(1 - y + 1/2k_i^2\lambda_D^2)^2} dy, \tag{2.40}$$

where $y \equiv \cos\theta$ and $G(y) = G(\cos\theta)$ is the overlap function in eq. (2.5). Also, m_f^* is the effective mass of the relevant band into which the holes are being scattered, k_i is the magnitude of the initial-state wave vector and $\hbar$ is the reduced Planck constant.

Nonpolar optical scattering: The nonpolar optical scattering which produces a perturbing potential by deforming the lattice and changing the band gap, is very important for holes. In

wide-band-gap-semiconductors, however, the optical phonon energy $\hbar\omega_0$ (on the order of 100 meV) is much greater than the thermal energy kT even at room temperature. The optical phonon energy in GaN (91 meV) is about three times that of GaAs (35 meV). This mechanism is quite important for holes in GaAs around room temperature. However, it is less important in GaN. The scattering rate is [17, 34, 35]

$$S_{npo}(\boldsymbol{k}_i, \boldsymbol{k}'_f) = \frac{D_{npo}^2 m_f^{*3/2}}{2\sqrt{2}\pi\rho\hbar^3\omega_0} \sum_{+,-} (E_i \pm \hbar\omega_0)^{1/2} \times \left(n_0 + \frac{1}{2} \mp \frac{1}{2}\right) \int_{-1}^{1} G(y)dy, \tag{2.41}$$

where D_{npo} is the optical phonon coupling constant, ρ is the density of semiconductor material, E_i is the initial hole energy and $n_0 = 1/[\exp(\hbar\omega_0/k_BT) - 1]$. ω_0, the longitudinal optical phonon angular frequency, is assumed to be constant. The signs in the summation, plus and minus, correspond to absorption and emission of an optical phonon, respectively. Note that the emission process can occur if the hole energy is higher than that of the optical phonons.

The optical phonon coupling constant D_{npo} is theoretically given by [17]

$$D_{npo} = \frac{\omega_0}{s} E_{npo}, \tag{2.42}$$

where s is the acoustic velocity and E_{npo} is the optical deformation potential which is about double E_1 in the case of GaAs [34]. Applying this concept to eq. (2.42) in the case of GaN, D_{npo} is found to be about 6.12×10^{11} eV/m. To confirm the effect of the scattering rate, the nonpolar optical scattering rate for D_{npo} using the values of 6.12×10^{11} and 1.0×10^{11} eV/m was calculated.

The mechanisms for polar optical scattering, acoustic deformation potential scattering and piezoelectric scattering are summarized briefly in Appendix C.

2.4.4 Relaxation time approximation and mobility

In order to determine drift (or conductivity) and Hall mobilities from the above-mentioned scattering mechanisms, the effective Hall factor using the "relaxation time approximation" have been determined. The effective Hall factor r_{eff} is [27]

$$r_{eff} = \frac{(1 + \alpha^{3/2})(r_1\alpha^{3/2}\beta^2 + r_2)}{(1 + \alpha^{3/2}\beta)^2}, \tag{2.43}$$

with $\alpha = m_1^*/m_2^*$, $\beta = \mu_1/\mu_2$, $\mu_i = e(\langle\tau_i\rangle/m_i^*)$ and $r_i = r_{Ai}(\langle\tau_i^2\rangle/\langle\tau_i\rangle^2)$. m_i^*, μ_i and τ_i are the effective masses, the drift mobilities and the relaxation times for the i-th hole band, respectively. (The index $i = 1$ always refers to heavy, and the index $i = 2$ to light holes.)

The relaxation and squares of relaxation times for the i-th hole band are determined by

$$\langle\tau_i^u\rangle = \frac{4}{3\pi^{1/2}} \int_0^\infty \left(\sum_{scat=1}^{n} \tau_{scat}^{-1}\right)^{-u} \frac{E^{3/2}}{(k_BT)^{5/2}} e^{-E/k_BT} dE, \tag{2.44}$$

where $u = 1$ is the relaxation time, $u = 2$ is the square of relaxation time, E is the hole energy and τ_{scat} is the inverse of the summation of the scattering rate of contributing mechanisms ($scat = 1, 2, \ldots, n$ corresponds to the different scattering mechanisms), including intraband, ii, and interband, if, and is given by

$$\tau_{scat} = \frac{1}{s_{ii}^{scat} + s_{if}^{scat}}. \tag{2.45}$$

The drift mobility μ is determined from relationships between drift and Hall mobilities given by

$$\mu = \frac{\mu_H}{r_{eff}}, \tag{2.46}$$

where μ_H is the Hall mobility and r_{eff} is the effective Hall factor given by eq. (2.43).

The theoretical Hall mobility, μ_H, is determined from eqs. (2.46) and (2.43) to be

$$\mu_H = \frac{e}{m_1^*} \frac{r_{A1}\langle\tau_1^2\rangle + \alpha^{1/2} r_{A2}\langle\tau_2^2\rangle}{\langle\tau_1\rangle + \alpha^{-1/2}\langle\tau_2\rangle}, \tag{2.47}$$

where m_1^* is the effective heavy-hole mass, and r_{A1} and r_{A2} are given in eq. (2.35).

The material parameters used in the hole transport calculations of the cubic phase of GaN are listed in Table 2.4.

2.4.5 Results: hole transport characteristics

Now first discuss the Hall coefficient anisotropy factors. Using Luttinger parameters, the valence band parameters (L, M, N, A, B, C) are determined, as listed in Table 2.3, for the first time. By using these valence band parameters, the anisotropy factors $r_{A1} = 0.668$ and $r_{A2} = 0.991$ are determined for the heavy- and light-hole bands, respectively as listed in in Table 2.5. For the comparison of these values, the anisotropy factors of GaAs are also listed. The anisotropy factor of the heavy-hole band results of a considerable reduction in $r_{A1} \ll 1$ but $r_{A2} \approx 1$ for the light hole band. To the extent, the transport properties of the valence band are dominated by $r_{A1} \ll 1$. Therefore it is evident that an effective r_A may be somewhat less than unity.

The temperature dependencies of scattering time by single-scattering mechanisms are plotted in Fig. 2.7. The interband scattering characteristic due to nonpolar optical phonons shown in Fig. 2.7(a) is different from that due to other scattering mechanisms shown in Figs. 2.7(b), 2.7(c) and 2.7(d). This is because the scattering relaxation time due to nonpolar optical phonon scattering is determined by the final-state effective hole mass (m_f^*), while that due to other scattering mechanisms is determined by both m_f^* and the magnitude of the initial state of the wave vector (k_i) in which nonparabolicity (see Appendix A) is considered. Two important conclusions can be deduced by comparing the magnitude of scattering time. First, the scattering mechanisms due to nonpolar optical phonons at all temperatures, and to polar optical phonons below 200 K, are not important to the hole transport characteristics because of their longer scattering time ($\gg 10^{-12}$ s). Second, at temperatures below 300 K, the acoustic deformation potential scattering mechanism plays the most important role.

Several approximations for the relaxation time of ionized impurity scattering have been proposed [36], however, there are no other theories more reliable than the Brooks-Herring (B-H) approximation. For the cubic phase of p-type GaN, the effective density of states in the valence band N_v is much larger than the total hole concentration p ($X_v = p/N_v \ll 1$) for the impurity concentration chosen here ($N_A = 5 \times 10^{17}$ cm^{-3}) with various compensation ratios ($K = 0.1, 0.5$ and 0.9) at temperatures between 50 and 400 K. Also, the screening length calculated by eq. (2.38) is much smaller than the interparticle distance. Thus the scattering rate of this mechanism, determined using the B-H approximation, is reasonable (small error) for a given N_A in this calculation [37]. To account for the uncertainty of acceptor activation energy, the average scattering time (τ_{av}) by ionized impurities is calculated for two activation energies (E_a=120 and 250 meV) with compensation ratios ($K = N_D/N_A$) between 0.1 and 0.9, and are plotted in Fig. 2.8. The acceptor concentration (N_A) is set to 5×10^{17} cm^{-3} in the calculations. τ_{av} is calculated using eq. (2.45) with τ_{scat}^{-1} as the sum of the scattering rate from heavy-to-heavy-hole, heavy-to-light-hole, light-to-light-hole and light-to-heavy-hole bands.

It goes without saying that the density of ionized impurities N_I ($=p + 2N_D$) in eq. (2.40) varied with temperature. Also, the values of N_Is are larger at an activation energy of 120 meV than those at activation energy of 250 meV with the same values of N_A and K, especially at higher temperatures. In the range of those acceptor activation energies (E_a=120 - 250 meV),

the effect of E_a on the average scattering time is almost negligible ($\tau_{av}(250)/\tau_{av}(120) \approx 1$ at 300 K) except for a low compensation ratio ($K = 0.1$). However, the effect of E_a on τ_{av} is appreciable ($\tau_{av}(250)/\tau_{av}(120) \approx 2$ at 300 K) at a low compensation ratio. It is also found that this scattering time characteristic is maintained even upon after decreasing E_a down to 100 meV.

The temperature dependence of Hall factors for the different phonon scattering mechanisms using r_{A1} and r_{A2} determined above are plotted in Fig. 2.9. The Hall factors for heavy hole- and light-hole bands of nonpolar and polar optical scattering vary as a function of temperature while those of the acoustic deformation potential and piezoelectric scattering are nearly constant. The temperature dependence of Hall factors can be attributed to the temperature dependence of the scattering relaxation time, since the changes in scattering relaxation times of nonpolar and polar optical scattering (change in scattering relaxation time $> 10^4$ s), as shown in Figs. 2.7(a) and 2.7(b), are larger than those of acoustic deformation potential and piezoelectric scattering (change in scattering relaxation time $\leq 10^2$ s) as shown in Figs. 2.7(c) and 2.7(d), in the calculated temperature range. The scattering relaxation time due to the acoustic deformation potential or piezoelectric scattering is not greatly affected by the temperature compared to that due to nonpolar or polar optical scattering. The values of the Hall factor for heavy-hole bands are lower than unity over the whole temperature range, because of the anisotropy factor effect. On the other hand, the Hall factor for light-hole bands varies from 1.0 to 1.5.

From the above results, the calculated Hall and drift mobilities due to the single lattice scattering mechanisms with the effective Hall factor as a function of temperature are shown in Fig. 2.10. It is obvious from the results that the acoustic deformation potential scattering is the most important mechanism limiting hole mobility in cubic phase GaN over a wide range of temperature (T=50 - 300 K). The calculation of the hole characteristics is mainly influenced by the uncertainty of several coupling constants that are currently not well known. Hence, the choice of parameter E_1 in eq. (C.2) is very important. Details are discussed later. For temperatures above 300 K, the polar optical phonon scattering mechanism is the dominant factor that influences hole transport characteristics. The inset in Fig. 2.10(a) shows the drift mobilities due to the acoustic phonon (dp) and piezoelectric scattering (pe) below 50 K. Based on this result, it should be noted that the calculation predicts that the piezoelectric scattering mechanism influences these characteristics, especially at low temperatures ($T \leq 50$ K).

The obtained effective Hall factors vary from 1.3 to 1.9 on changing the temperature as shown in Fig. 2.10(b). This result indicates that the Hall factors become increasingly important with increasing temperature when we attempt to compare the calculated drift mobility with measured Hall ones.

Considering the ionized impurity scattering, as well as the lattice scattering mechanisms, the calculated Hall and drift mobilities and the effective Hall factor as a function of temperature with compensation ratios (K) between 0.0 and 0.9 are plotted in Fig. 2.11. The acceptor concentration of $N_A = 5 \times 10^{17}$ cm^{-3} and E_a=120 meV are used in this calculation.

As the compensation ratio (K) increases, the temperature at maximum mobility also increases. The effective Hall factor (r_{eff}) increases as K decreases with increasing temperature. From Figs. 2.11(a) and 2.11(b), it is observed that the maximum value of the Hall and drift mobilities are in the temperature range 80 - 150 K for all values of K between 0.1 and 0.9. In comparison with Fig. 2.10(b), Fig. 2.11(b) shows that the inclusion of scattering by ionized impurities into the Hall factor calculation is important at high compensation ratio (K=0.5 and 0.9). The obtained effective Hall factors vary from 1.4 to 1.8 with changing temperature ($K \geq 0.1$). The ionized impurity scattering mechanism affects the temperature at minimized effective Hall factor and the effective Hall factor itself.

The Hall and drift mobilities as a function of total hole concentration (p) with compensation ratios (K) between 0.1 and 0.9 for E_a=120 and 250 meV at 300 K are plotted in Figs. 2.12(a) and 2.12(b). In the calculations, the acceptor concentrations (N_A) were varied from 1×10^{16} cm^{-3} to 8×10^{18} cm^{-3} for each K. The total hole concentrations determined by eq. (2.39) for E_a= 120 meV and 250 meV are 2.9×10^{17} cm^{-3} and 2.7×10^{15} cm^{-3} (K=0.1, N_A=8×10^{18} cm^{-3}), respectively.

One of the most important properties derived from Hall measurement is the mobility characteristic as a function of carrier concentration. It is found that the mobilities at E_a=250 meV change drastically for a small change of hole concentration (p); however, those at E_a=120 meV change gradually with increasing p. Quantitatively, the maximum Hall and drift mobilities calculated here are about 315 $cm^2V^{-1}s^{-1}$ and 175 $cm^2V^{-1}s^{-1}$, respectively. The Hall mobilities decrease from 315 $cm^2V^{-1}s^{-1}$ at low hole concentrations to about 171 $cm^2V^{-1}s^{-1}$ at hole concentration of 3×10^{17} cm^{-3} at E_a=120 mV and $K = 0.1$. This also shows clearly that the compensation ratio is strongly affects the hole transport characteristics. The mobility abruptly decreases with increasing K. This indicates that the use of cubic-phase GaN in devices is thought to be limited by the compensation ratio. If the compensation ratio varies from 0.1 to 0.5 at a hole concentration p of 2.6×10^{16} cm^{-3}, the Hall mobility changes from 302 to 259 $cm^2V^{-1}s^{-1}$ (E_a=120 mV).

Knowledge of the anisotropy parameter is essential for the evaluation of hole transport characteristics. Figure 2.13 shows how the drift mobility and the effective Hall factor deviated on using unity values of r_{A1} and r_{A2} and values calculated by us ($r_{A1} = 0.668$ and $r_{A2} = 0.991$). It is clear seen from this that the influence of the anisotropy parameter on the drift mobility is strong at all calculated temperature ranges. The theoretical drift mobility with the calculated value of r_{Ai} is half that with a unity value of r_{Ai}. Thus, it is necessary to account for the correct anisotropy parameters for the effective Hall factor when the comparing theory and actual Hall measurement.

Finally, we investigated the influence of E_1 and D_{npo} of ambiguous values, as mentioned earlier (§2.4.1, §2.4.5). As mentioned before, the hole transport characteristics depend on the uncertainty of coupling constants. To investigate the influence of these values, we performed hole transport calculations at the acceptor concentration of $N_A = 5 \times 10^{17}$ cm^{-3}, E_a=120 meV and compensation ratio K=0.5. Figure 2.14 shows how E_1 influenced the Hall mobility and the effective Hall factor. Based on this result, we find that if the constant for E_1 is varied by ±20%, the deviation of the resulting Hall mobility is about 22% at 300 K. Thus, E_1 is the important parameter for calculating the mobility.

In the case of constant D_{npo}, Fig. 2.15 shows how D_{npo} influenced on Hall and the effective Hall factor, using the values of $D_{npo} = 1.0 \times 10^{11}$ eV/m and 6.1×10^{11} eV/m estimated by applying the theory to the case of GaAs. Although this ambiguity slightly affected hole transport only at high temperatures (T ≥ 150 K), in general, the variation of this constant is not greatly affected. This result is easily understood, since the nonpolar optical phonon scattering is not the predominant mechanism which affects the mobility characteristics, as seen in Fig. 2.10(a).

2.5 Conclusions

The Monte Carlo simulation program is developed and the simulations are performed to compare the transit times, velocity overshoot effects, and applied electric field and temperature dependence of velocity in cubic and hexagonal phases of GaN and GaAs.

Overshoot effects dominate and the transit time in both phases GaN is comparable or less than that of GaAs in shorter distance. And the transit time are less than those in GaAs with distances shorter than 0.2 μm.

In comparison with hexagonal phase GaN, the cubic phase GaN has an advantage from the applied field electric dependent and temperature dependent velocity field. Furthermore, both phases may be capable of same or higher frequency performance than GaAs when transit time is an important factor.

The theoretical Hall and drift mobilities, and the effective Hall factor of the cubic phase of p-type GaN were calculated, for the first time, over a wide range of temperatures (T=50 - 400 K) using the "relaxation time approximation".

The valence band parameters for the light- and heavy-hole band energy surfaces were determined. Then the anisotropy factors for heavy- and light-hole bands were also calculated using Luttinger and valence band parameters.

The quantitative explanation of the anisotropy factors which determine hole mobilities was shown. The results of calculations showed that scattering by the acoustic deformation potential plays an important role in determining the hole transport characteristics at temperatures between 50 and 300 K.

Concerning the ambiguity of the activation energies in the ionized impurity scattering mechanism, there is no significant difference in the scattering time in the range 100 - 250 meV at high compensation ratios (K=0.5 and 0.9).

The theoretical Hall mobilities at total hole concentrations of 3.5×10^{15} ($N_A = 8\times10^{15}$ cm^{-3}) and 3.5×10^{16} cm^{-3} ($N_A = 5 \times 10^{17}$ cm^{-3}) are about 312 and 225 cm^{2}V^{-1}s^{-1}, respectively, with the activation energy of 120 meV and the compensation ratio of 0.5 at 300 K.

A rather important conclusion is that the hole transport characteristics are strongly affected by the compensation ratio. This becomes marked as the carrier concentration is increase.

Unfortunately, the calculated Hall mobility is still higher than that in the experimental reports, but may approach that value if the quality of the cubic phase of GaN film is improved.

A future study will explore this issue.

Table 2.1: Material parameters of cubic phase of GaAs, cubic phase of GaN and hexagonal phase of GaN in the Monte Carlo simulations.

Property	Symbol	Units	Cubic GaAs	Cubic GaN	Hexagonal GaN
Dielectric constant	ε_s		12.9[a)]	9.5[b)]	9.5[b)]
	ε_∞		10.9[a)]	5.35[b)]	5.35[b)]
Density	ρ	kg/m^3	5360[a)]	6095[b)]	6095[b)]
Sound velocity	s	m/s	3860[a)]	4570[b)]	4330 [b)]
Acoustic deformation potential	E_1	eV	9.3[a)]	10.1[b)]	8.3[c)]
Equivalent inter valley deformation potential	D_{ij}	$\times 10^{11}$ eV/m	50.[e)]	0.5[f)]	0.5[d)]
Nonequivalent inter valley deformation potential	D_{ij}	$\times 10^{11}$ eV/m	1.0[e)]	1.0[f)]	1.0[d)]
Polar optical phonon energy	$\hbar\omega_0$	eV	0.0354[a)]	0.092[b)]	0.092[b)]
Piezoelectric constant	h_{pz}	C/m^2	0.14[a)]	0.375[d)]	0.56[c)]

[a)] Reference [17].
[b)] Reference [22].
[c)] Reference [6].
[d)] Reference [13].
[e)] Reference [16].
[f)] Assumed to be same as values of hexagonal because of no available data.

Table 2.2: Valley parameters of cubic phase of GaAs, cubic phase of GaN and hexagonal phase of GaN in the Monte Carlo simulations.

Material	Valley	Energy gap (eV)	Electron effective mass (m_0)	Nonparabolicity (eV^{-1})
GaAs	1	1.493	0.063	0.651
	2	1.709	0.222	0.455
	3	1.900	0.580	0.221
Cubic GaN	1	3.4	0.15	0.250
	2	4.7	0.40	0.128
	3	6.0	0.60	0.067
Hexagonal GaN	1	3.5	0.19	0.231
	2	5.5	0.40	0.109
	3	5.6	0.60	0.714

Table 2.3: Valence band parameters for the cubic phase GaN.

Material	γ_1	γ_2	γ_3	$-L$	$-M$	$-N$	$-A$	$-B$	C^2
GaN	3.07	0.86	1.26	2.35	7.51	7.56	3.07	1.72	10.18

Note: The notation of parameters used here are same those in ref. [27].

Table 2.4: Bulk material parameters of cubic phase GaN used in the calculation.

Property		Units	Value
E_g	Energy gap	eV	3.38[a)]
m_1/m_0	Effective heavy hole mass ratio		0.76[a)]
m_2/m_0	Effective light hole mass ratio		0.21[a)]
ρ	Density	kg/m^3	6095[b)]
s	Sound velocity	m/s	4570[b)]
E_1	Acoustic deformation potential	eV	10.1[b)]
D_{npo}	Optical coupling constant	ev/m	1.0×10^{11}[b)]
ε_s	Static dielectric constant		9.5[b)]
ε_∞	High frequency dielectric constant		5.35[b)]
$\hbar\omega_0$	Polar optical phonon energy	eV	0.0912[c)]
h_{pz}	Piezoelectric constant	C/m^2	0.375[c)]

[a)] Reference [25].
[b)] Reference [22].
[c)] Reference [37].

Table 2.5: Anisotropy parameters for the cubic phase GaN and GaAs.

Material	Heavy-hole band	Light-hole band
	r_{A1}	r_{A2}
GaN	0.668	0.991
GaAs	0.659	0.998

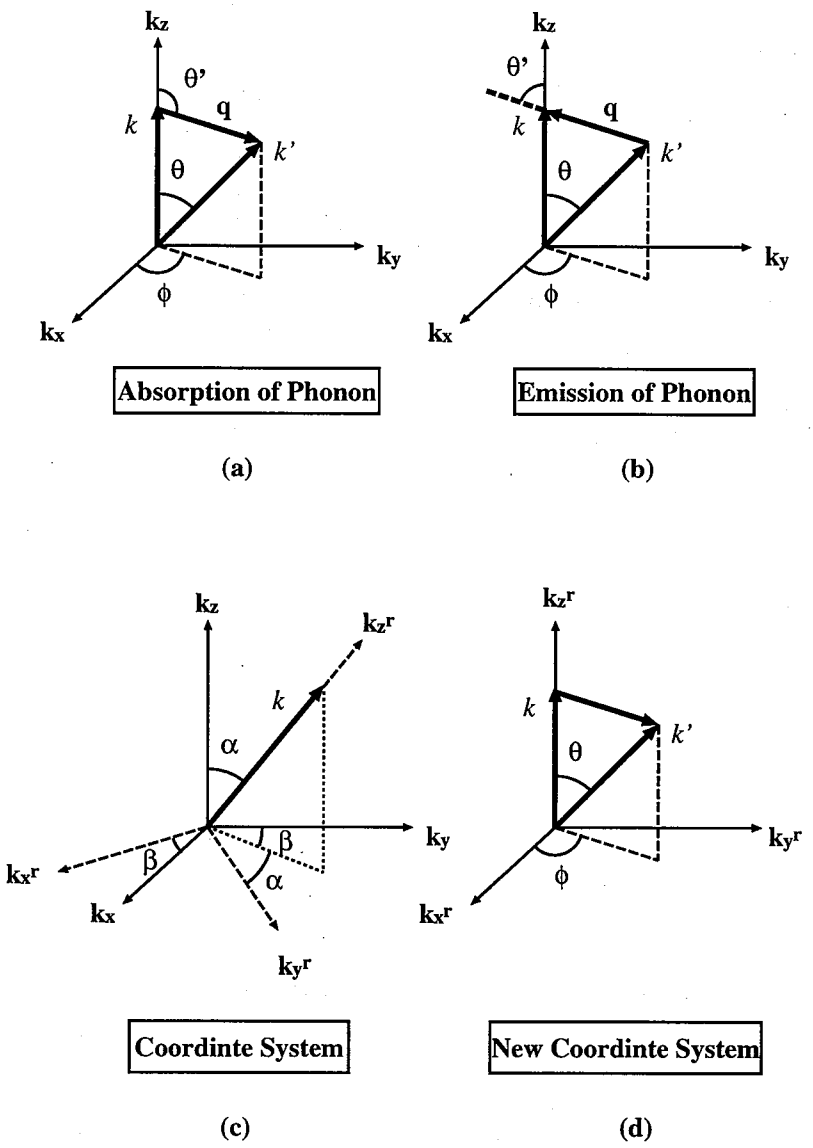

Figure 2.1: Relationship between the various wave vectors involved in electron/hole scattering by a phonon (a), (b) and geometry for the determination of the state after scattering when full three-dimensional simulation performed (c), (d).

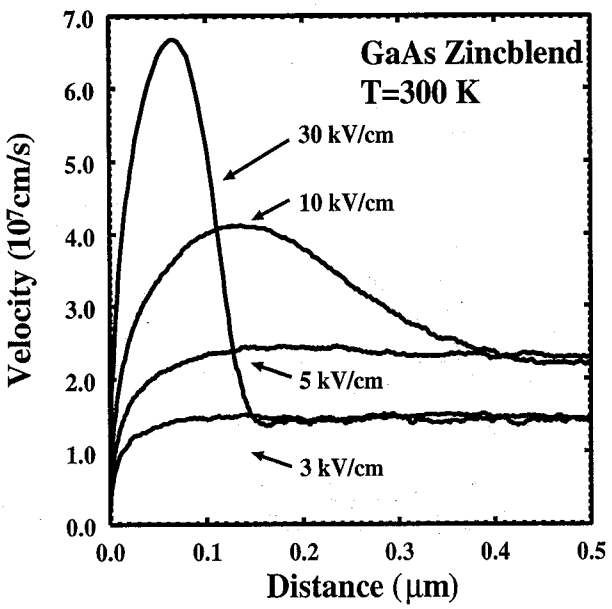

(a) Cubic GaAs.

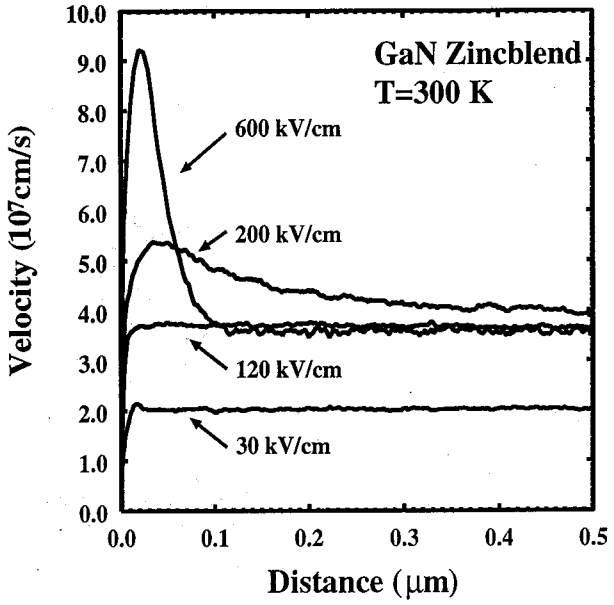

(b) Cubic GaN.

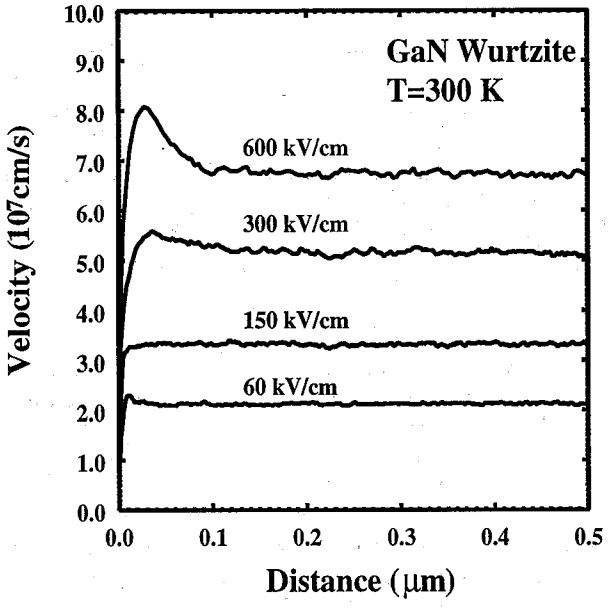

(c) Hexagonal GaN.

Figure 2.2: Monte Carlo simulation of electron velocity as a function of distance in cubic phase of GaAs, cubic phase of GaN and hexagonal GaN.

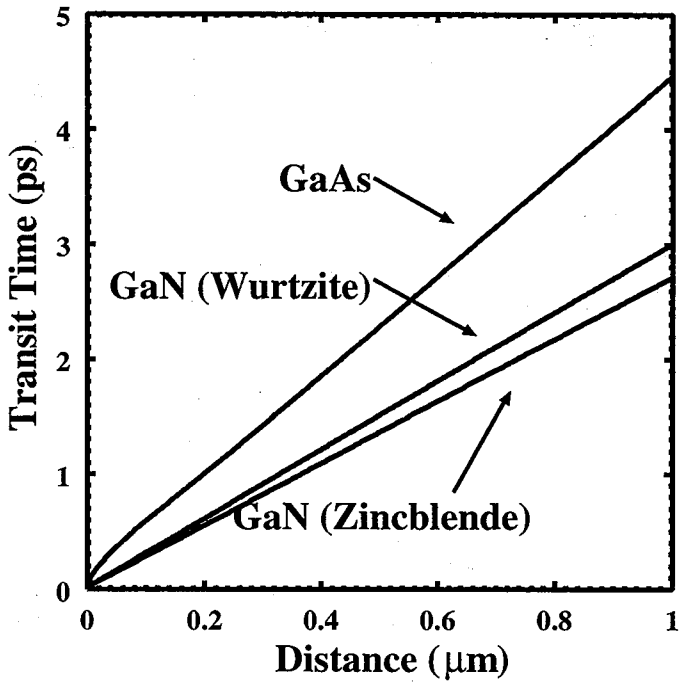

Figure 2.3: Electron transit time as a function of distance. The calculated fields are 5 kV/cm (GaAs), 120 kV/cm (cubic GaN) and 150 kV/cm (hexagonal GaN).

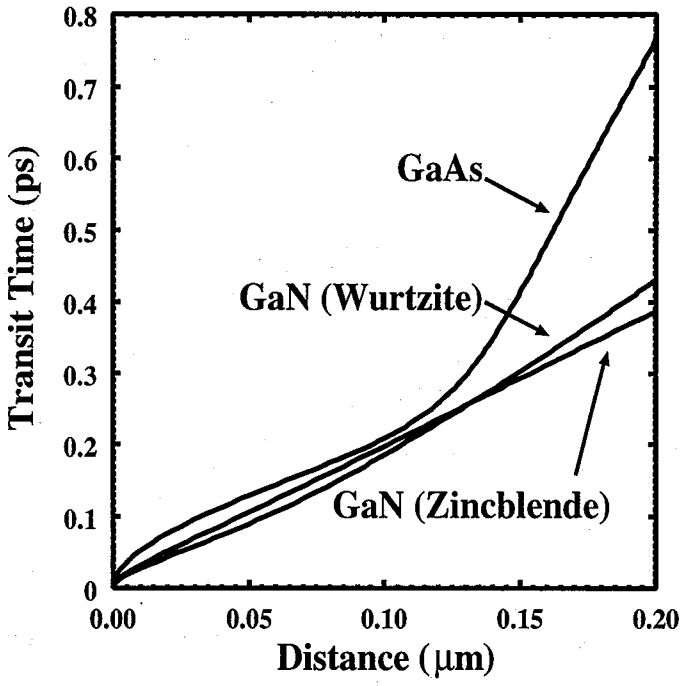

Figure 2.4: Electron transit time as a function of distance across 0.2 μm (overshoot regime). The calculated fields are 30 kV/cm (GaAs), 300 kV/cm (cubic GaN) and 300 kV/cm (hexagonal GaN).

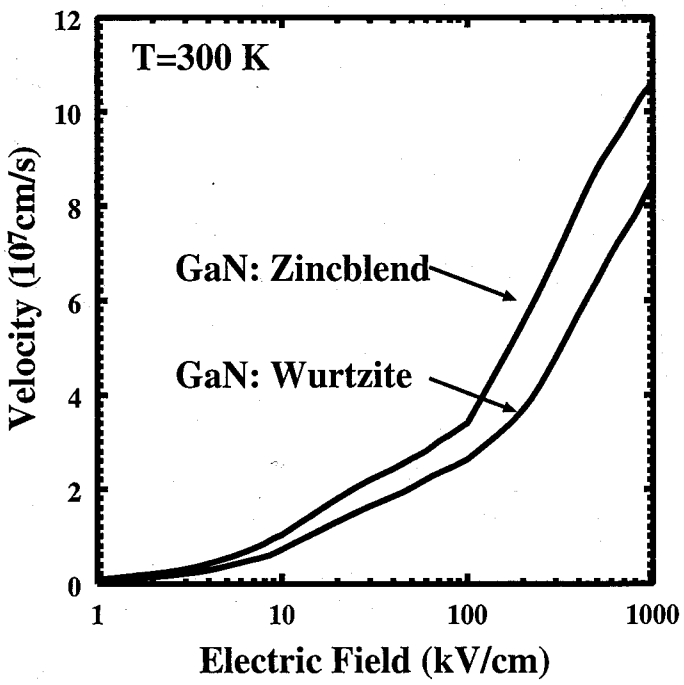

Figure 2.5: Peak electron velocity for both cubic and hexagonal phase of GaN as a function of applied fields (10 - 1000 kV/cm). The temperature is set to 300 K.

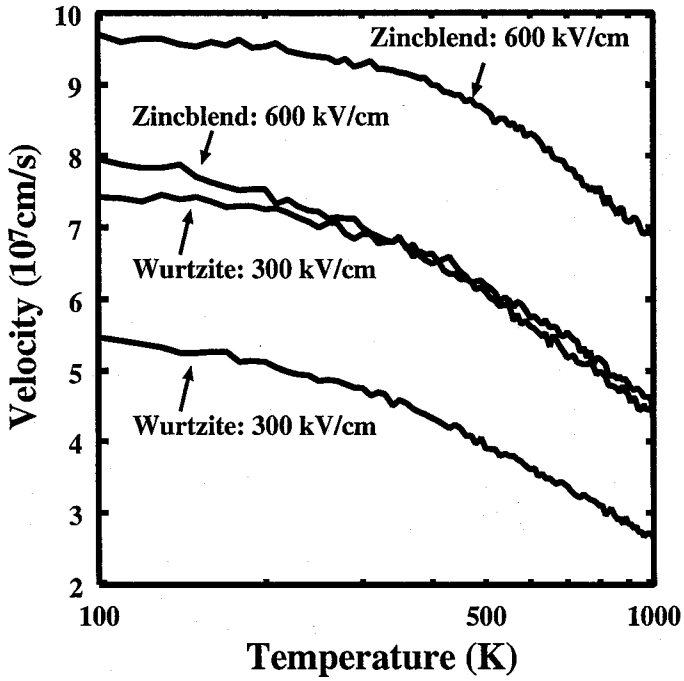

Figure 2.6: Electron velocity as a function of temperature (100 - 1000 K). The calculated fields are 300 kV/cm and 600 kV/cm for both cubic and hexagonal phase of GaN.

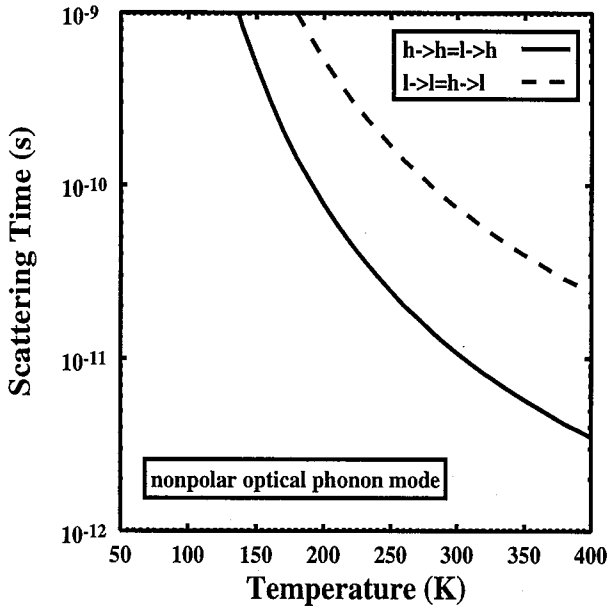

(a) Nonpolar optical phonon mode (*npop*).

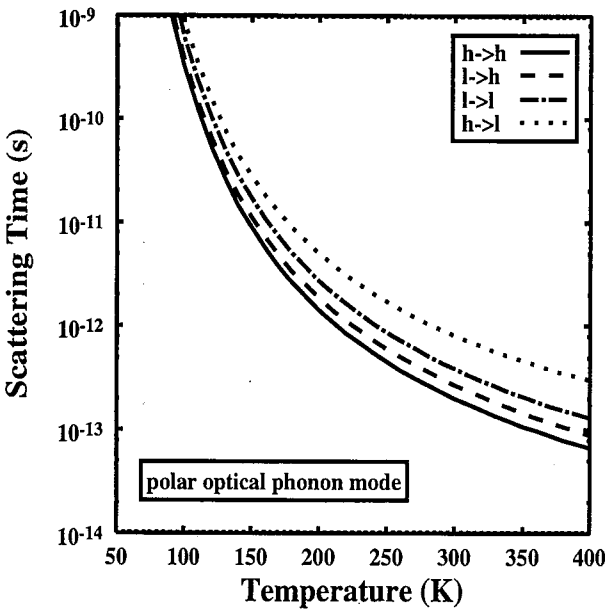

(b) Polar optical phonon mode (*pop*).

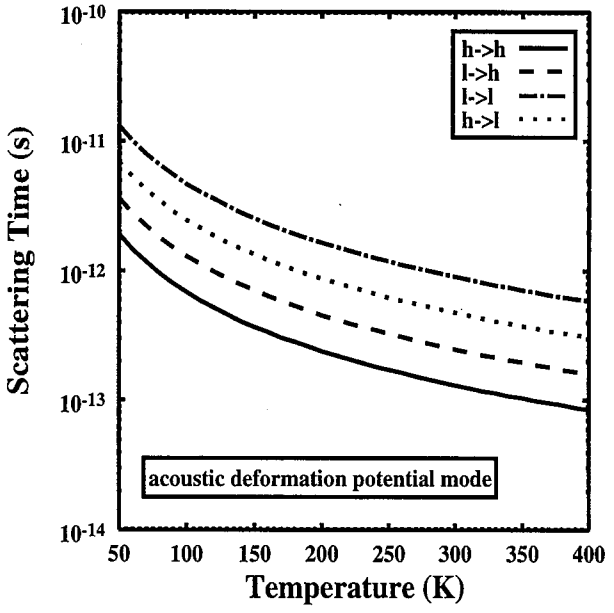

(c) Acoustic deformation potential mode (*dp*).

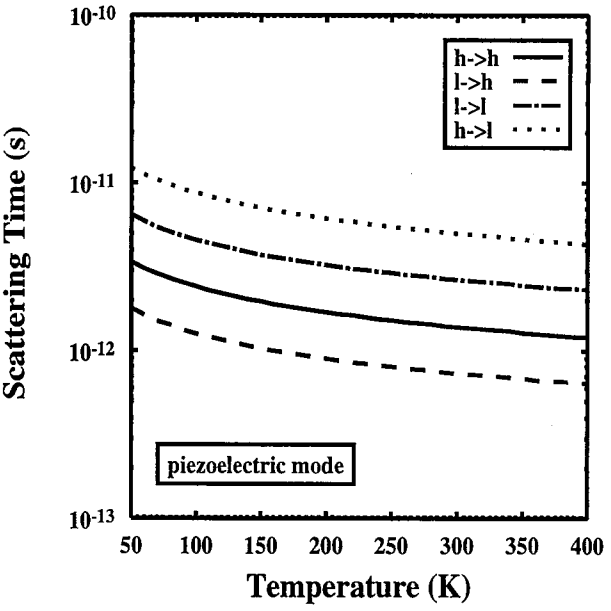

(d) Piezoelectric mode (*pz*).

Figure 2.7: Variation with temperature of calculated scattering relaxation time corresponding to nonpolar optical phonon mode (a), polar optical phonon mode (b), acoustic deformation potential mode (c) and piezoelectric mode (d). (h→h - scattering from heavy-to-heavy-hole band, h→l - scattering from heavy-to-light-hole band, l→l - scattering from light-to-light-hole band, and l→h - scattering from light-to-heavy-hole band.)

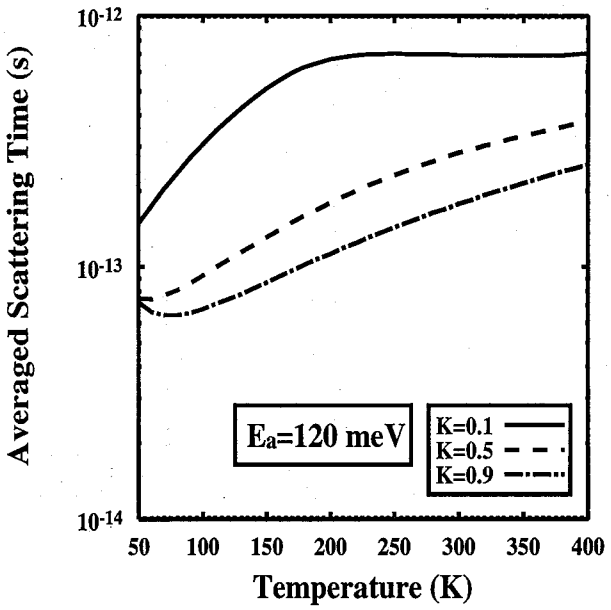

(a) Average scattering time for ionized impurity scattering with temperature for E_a=120 meV.

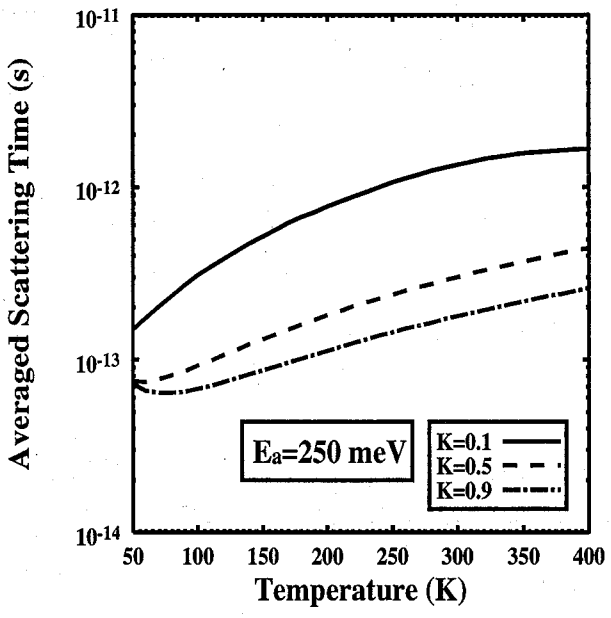

(b) Average scattering time for ionized impurity scattering with temperature for E_a=250 meV.

Figure 2.8: Variation of calculated averaged scattering time for ionized impurity scattering with temperature for E_a=120 and 250 meV with dependence on compensation ratio (K=N_D/N_A). The acceptor concentration (N_A) was set to 5 $\times 10^{17}$ cm^{-3} in the calculations.

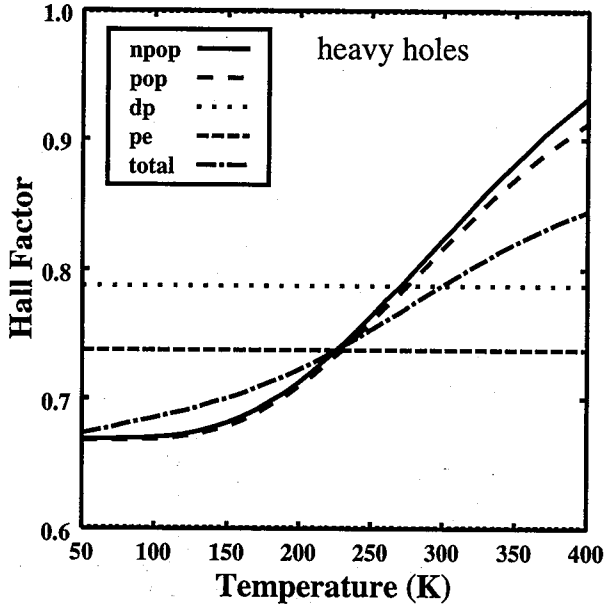

(a) Effective Hall factors with temperature due to lattice scattering mechanisms for heavy hole.

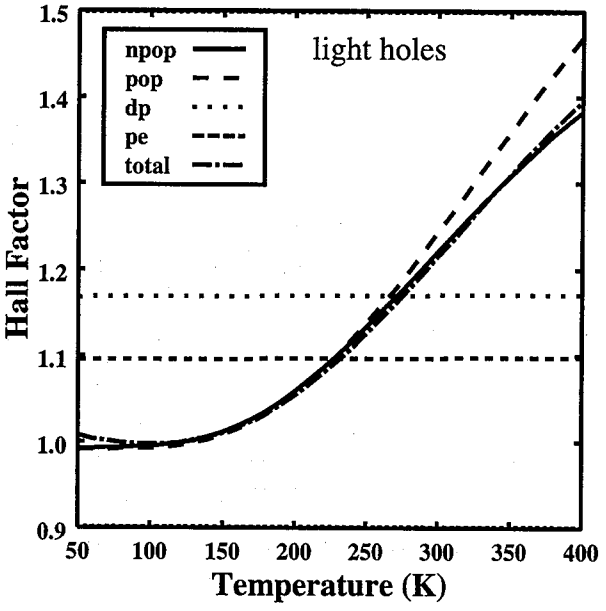

(b) Effective Hall factors with temperature due to lattice scattering mechanisms for light hole.

Figure 2.9: Variation of calculated effective Hall factors with temperature due to lattice scattering mechanisms for heavy holes (a) and for light holes (b). *npop* is the nonpolar optical phonon scattering. *pop* is the polar optical phonon scattering. *dp* is the acoustic phonon scattering. *pe* is the piezoelectric scattering. *total* is the total of all four lattice scattering mechanisms.

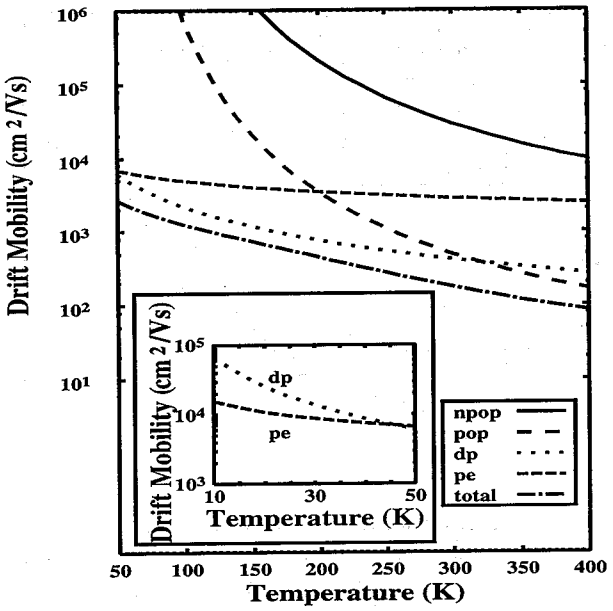

(a) Drift mobilities due to each lattice scattering mechanisms.

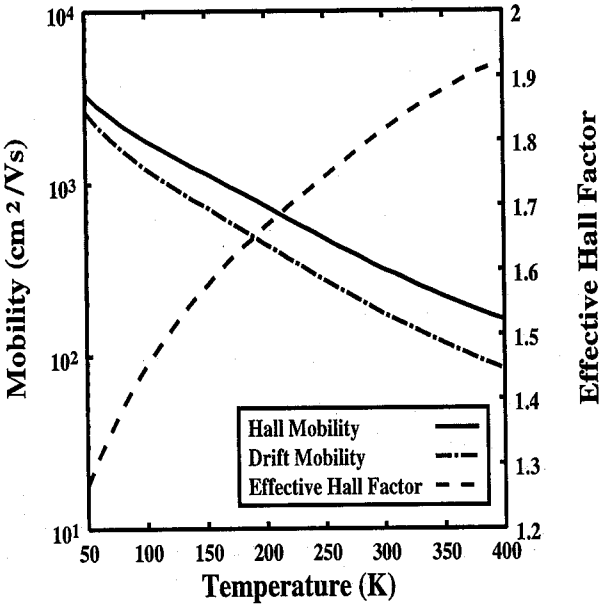

(b) Hall and drift mobilities and the effective Hall factor due to lattice scattering mechanisms.

Figure 2.10: Theoretical drift mobilities due to each lattice scattering mechanisms (a), and the theoretical Hall and drift mobilities and the effective Hall factor (b) due to lattice scattering mechanisms as a function of temperature. The inset in (a) shows the drift mobilities due to *dp* and *pe* below 50 K.

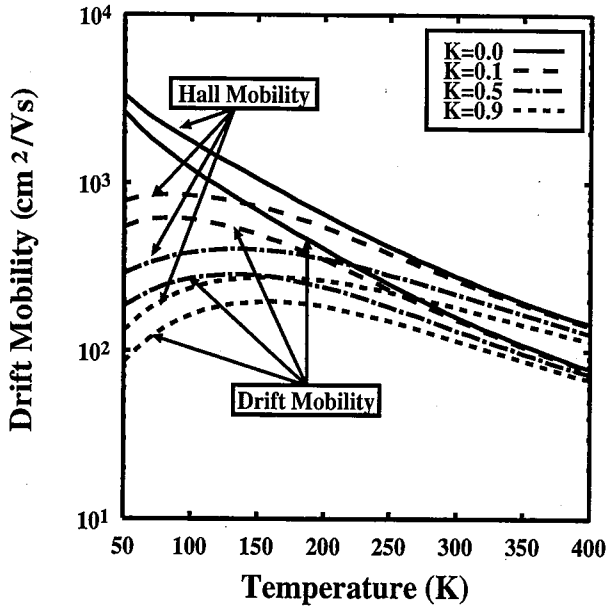

(a) Hall and drift mobilities due to lattice and ionized impurity scattering mechanisms.

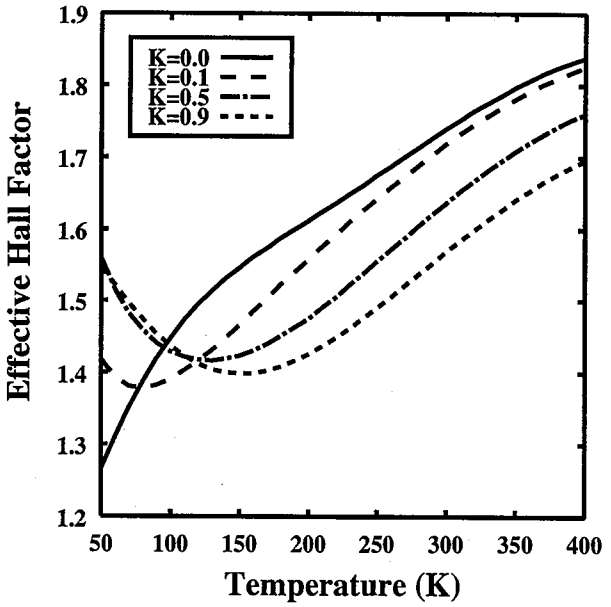

(b) Effective Hall factor due to lattice and ionized impurity scattering mechanisms.

Figure 2.11: Theoretical Hall and drift mobilities (a), and effective Hall factor (b) due to lattice and ionized impurity scattering mechanisms for different ratio of compensation as a function of temperature. E_a used in the ionized impurity scattering mechanism is 120 meV.

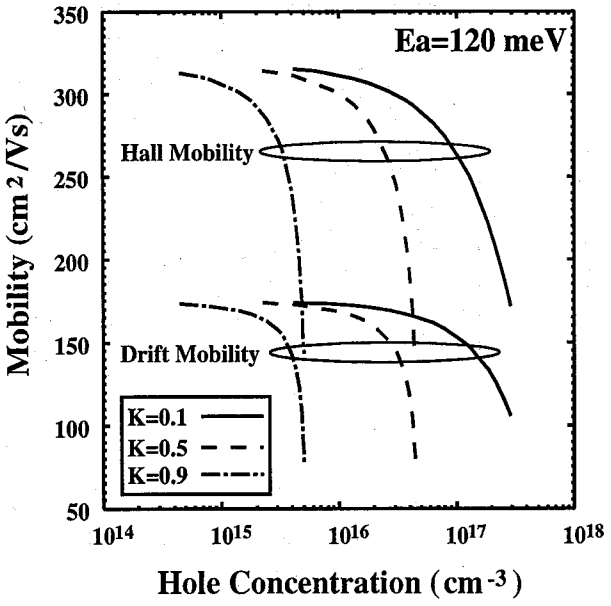

(a) Hall and hole mobilities for E_a=120 meV.

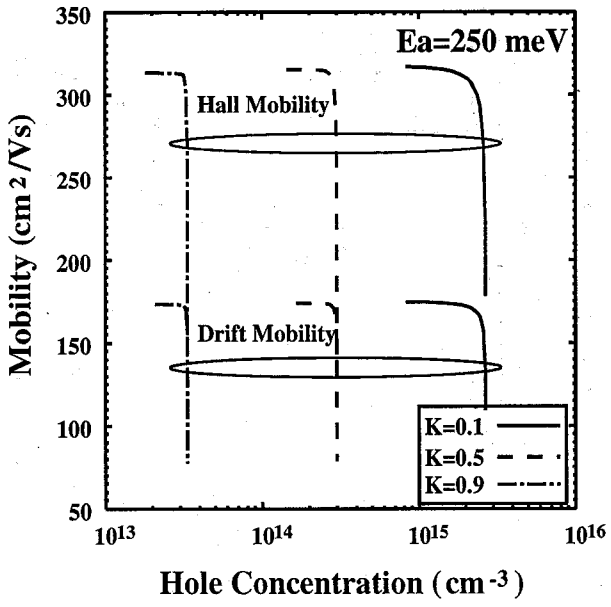

(b) Hall and hole mobilities for E_a=250 meV.

Figure 2.12: A comparison of theoretical Hall and hole mobilities as a function of total hole concentration with compensation ratio (K=N_D/N_A) of 0.1, 0.5 and 0.9 for E_a=120 (a) and 250 meV (b) at 300 K.

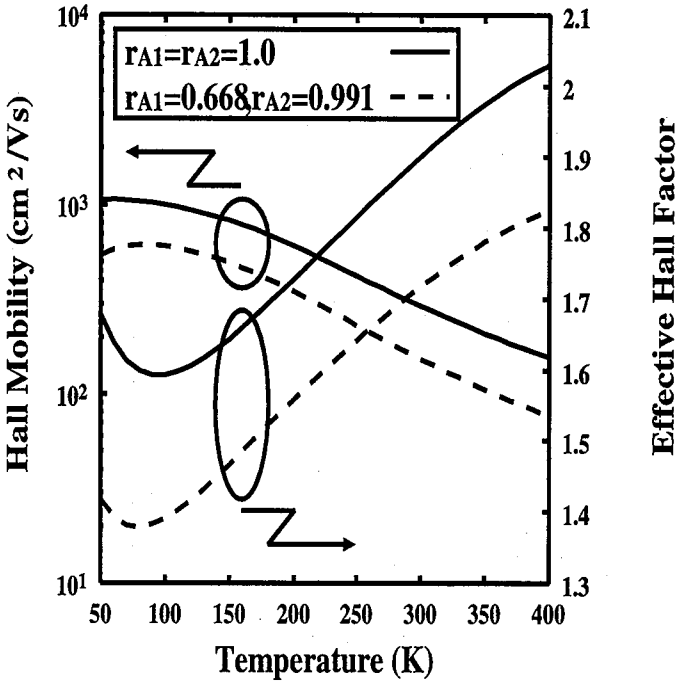

Figure 2.13: Theoretical Hall mobility and effective Hall factor as a function of acceptor concentration, comparing the choice of anisotropy parameters.

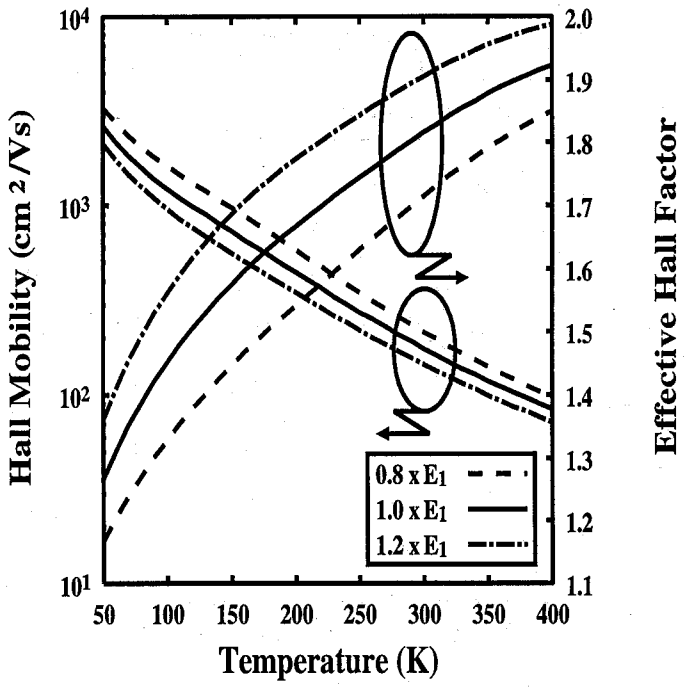

Figure 2.14: Theoretical Hall mobility and effective Hall factors as a function of temperature, comparing the choice of the acoustic deformation potential constant E_1. The lattice scattering mechanisms *npop*, *pop*, *dp* and *pe* are considered in the calculation.

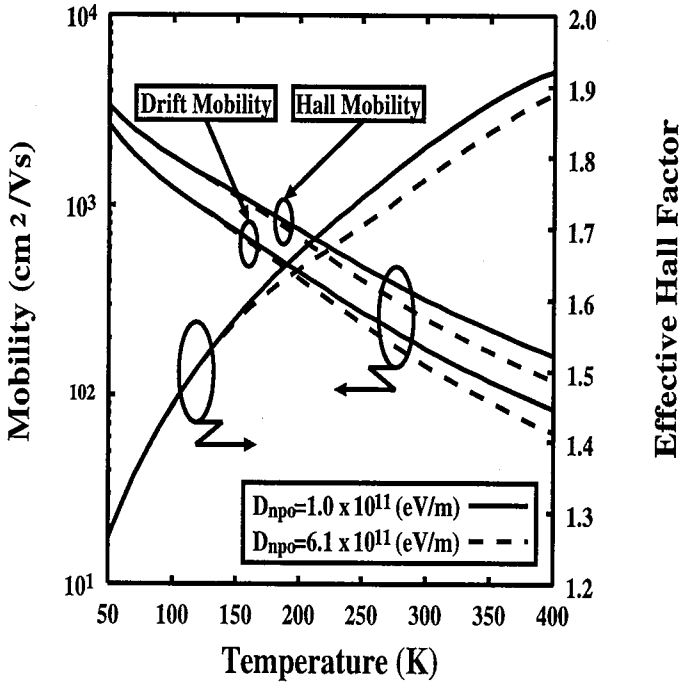

Figure 2.15: Theoretical Hall mobility and effective Hall factors as a function of temperature, comparing the choice of the deformation potential constant D_{npo}. The lattice scattering mechanisms *npop*, *pop*, *dp* and *pe* are considered in the calculation.

Appendix A

Kane Model and Nonparabolicity

In the Kane model [24], the energy band is represented by a nonparabolic, spherical, and analytical effective mass expression of the following form:

$$\frac{\hbar^2 k^2}{2m^*} = E(1+\alpha E), \tag{A.1}$$

where $\hbar k$ denotes the crystal momentum, E represents the electron/hole energy, m^* is the effective mass, and the nonparabolicity coefficient, α, is given by

$$\alpha = \frac{1}{E_g}\left(1-\frac{m^*}{m_0}\right)^2, \tag{A.2}$$

where m_0 and E_g denote the bare electron mass and the energy gap.

Appendix B

Determination of Γ, a_d, a_{11} and a_{12}

Together with the valence band parameters A, B and C discussed in §2.4.2, Γ is given by [27]

$$\Gamma = \mp \frac{C^2}{2B'(A \pm B)}, \tag{B.1}$$

where B' is the $(B^2 + C^2/6)^{1/2}$.

a_d, a_{12} and a_{11} are determined by following approximate forms.

$$a_d = 1 + 0.05\Gamma + 0.01635\Gamma^2 + 0.000908\Gamma^3 + \cdots \tag{B.2}$$

$$a_{11} = 1 + 0.01667\Gamma + 0.041369\Gamma^2 + 0.00090679\Gamma^3 + 0.00091959\Gamma^4 + 0.00002106\Gamma^5 + \cdots \tag{B.3}$$

$$a_{12} = 1 - 0.01667\Gamma + 0.017956\Gamma^2 - 0.0069857\Gamma^3 + 0.0012610\Gamma^4 + \cdots \tag{B.4}$$

Appendix C

Other Scattering Mechanisms in Hole Transport Calculation

The expressions for scattering mechanisms, except other than those mentioned in §2.4.4, are summarized.

Polar optical scattering: The polar optical scattering mechanism, which is the interaction between free holes by dipole moment, is the most important at room temperature. The scattering rate is [17, 34]

$$S_{po}(\boldsymbol{k}_i, \boldsymbol{k}'_f) = \frac{e^2 m_f^* \omega_0}{4\pi\varepsilon_s \hbar^2}\left(\frac{1}{\varepsilon_\infty} - \frac{1}{\varepsilon_s}\right)\frac{1}{k_i^2}\left(\sum_{+,-} k_\pm \left(n_0 + \frac{1}{2} \mp \frac{1}{2}\right)\right.$$
$$\left. \times \int_{-1}^{1} \frac{G(y)}{1 - 2(k_\pm/k_i) + (k_\pm/k_i)^2} dy\right), \tag{C.1}$$

where ε_∞ is the high-frequency dielectric constant. The wave vectors $k_\pm$ correspond to energies $E_i \pm \hbar\omega_0$, respectively.

Acoustic deformation potential scattering: The acoustic deformation potential due to the changing of lattice atom positions scatters carriers. The scattering rate by acoustic deformation potential is given by the form [17, 34]

$$S_{ac}(\boldsymbol{k}_i, \boldsymbol{k}'_f) = \frac{E_1^2 k_B T m_f^*}{\pi\rho\hbar^3 s^2} k_i \int_{-1}^{1} \frac{G(y)}{2} dy, \tag{C.2}$$

where E_1 is the acoustic deformation potential.

Piezoelectric scattering: The scattering rate by the piezoelectric potential has the form [17, 34]

$$S_{pz}(\boldsymbol{k}_i, \boldsymbol{k}'_f) = \frac{e^2 h_{pz}^2 k_B T m_f^*}{2\pi\hbar^3 s^3 \varepsilon_s^2}\frac{1}{k_i}\int_{-1}^{1} \frac{G(y)}{2} dy, \tag{C.3}$$

where h_{pz} is the piezoelectric constant. Sometimes e_{14} is used instead of h_{pz}. In most other III–V semiconductors such as GaAs, the effect of this scattering mechanism on hole transport is less important than that of the other scattering mechanisms.

Bibliography

[1] M. E. Lin, G. Xue, G. L. Zhou, J. E. Green and H. Morkoc: Appl. Phys. Lett. **63** (1993) 932.

[2] S. Chichibu, H. Okumura, S. Nakamura, G. Feuillet, T. Azuhata, T. Sota and S. Yoshida: Jpn. J. Appl. Phys. **36** (1997) 1976.

[3] B. E. Foutz, L. F. Eastman, U. V. Bhapkar and M. S. Shur: Appl. Phys. Lett. **70** (1997) 2849.

[4] P. Das and D. F. Ferry: Solid State Electron. **19** (1976) 851.

[5] W. Seifert and A. Tempel: Phys. Status Solidi **A23** (1974) K39.

[6] S. K. O'Leary, B. E. Foutz, M. S. Shur, U. V. Bhapkar and L. F. Eastman: J. Appl. Phys. **83** (1998) 826.

[7] M. A. Littlejohn, J. R. Hauser and T. H. Glisson: Appl. Phys. Lett. **11** (1975) 625.

[8] B. Gelmont, K. Kim and M. Shur: J. Appl. Phys. **74** (1993) 1818.

[9] V. W. L. Chin, T. R. Tansley and T. Osotchan: J. Appl. Phys. **75** (1994) 7365.

[10] N. S. Mansour, K. W. Kim and M. A. Littlejohn: J. Appl. Phys. **77** (1995) 2834.

[11] U. V. Bhapkar and M. S. Shur: J. Appl. Phys. **82** (1997) 1649.

[12] J. D. Albrecht, R. P. Wang, P. P. Ruden, M. Farahmand and K. F. Brennan: J. Appl. Phys. **83** (1998) 1446.

[13] J. D. Albrecht, R. P. Wang, P. P. Ruden, M. Farahmand and K. F. Brennan: J. Appl. Phys. **83** (1998) 4777.

[14] B. K. Ridley: *Quantum Processes in Semiconductors* (Oxford University Press, Oxford, 1988) 2nd ed.

[15] D. K. Ferry: *Semiconductors* (Macmillian, New York, 1991).

[16] K. Tomizawa: *Handotai Debaisu Shimyuresyon* (Semiconductor Device Simulation) (Korona, Tokyo, 1996) p. 208 [in Japapnese].

[17] M. Wenzel, G. Irmer, J. Monecke and W. Siegei: J. Appl. Phys. **81** (1997) L7810.

[18] R. P. Joshi: Appl. Phys. Lett. **64** (1994) 223.

[19] C. Jacoboni and L. Reggiani: Rev. Mod. Phys. **55** (1983) 645.

[20] P. Lugli and D. K. Ferry: IEEE Trans. Electron. Devices **ED-32** (1985) 2431.

[21] M. V. Fischetti and S. E. Laux: Phys. Rev. **38** (1988) 9728.

[22] J. Kolnik, I. H. Oguzman, K. F. Brennan, R. Wang, P. Ruden and Y. Wang: J. Appl. Phys. **78** (1995) 1033.

[23] L. V. Keldysh: ZhTETF **48** (1965) 1962.

[24] W. Fawcett, A. D. Boardman and S. Swain: J. Phys. Chem. Solids **31** (1970) 1963.

[25] W. F. Fan, M. F. Li, T. C. Chong and J. B. Xia,: Solid State Commun. **97** (1996) 381.

[26] M. Suzuki and T. Uenoyama: Mater. Res. Soc. Symp. Proc. **468** (1997) 251.

[27] J. D. Wiley: *Semiconductors and Semimetals* (Academic, New York, 1975) Vol. 10, Chap. 2.

[28] G. Dresselhaus, A. F. Kip and C. Kittel: Phys. Rev. **98** (1955) 368.

[29] B. Lax and J. G. Mavroides: Phys. Rev. **100** (1955) 1650.

[30] A. C. Beer: *Galvanomagnetic Effects in Semiconductors* (Academic, New York, 1963).

[31] R. J. Stirn: *Semiconductors and Semimetals* (Academic, New York, 1972) Vol. 8.

[32] H. Brooks and C. Herring: Phys. Rev **83** (1951) 879.

[33] O. Brandt, H. Yang, H. Kostial and K. Ploog: Appl. Phys. Lett. **71** (1996) 2707.

[34] D. C. Look, D. K. Lorance, J. R. Sizelove, C. E. Stutze, K. R. Evans and D. W. Whitson: J. Appl. Phys. **71** (1992) L260.

[35] T. Brudevoll, T. A. Fjeldy, J. Baek and M. S. Shur: J. Appl. Phys. **67** (1990) L7373.

[36] D. Chattopadhyay and H. J. Queisser: Rev. Mod. Phys. **53** (1981) 745.

[37] M. Shur, B. Glemont and M. Asifkhan: J. Electron. Mater. **25** (1996) 777.